JGR Atmospheres

RESEARCH ARTICLE
10.1029/2018JD029508

Key Points:
- Radiomteric measurements from two Atmospheric Radiation Measurement program field campaigns, held in dry locations, have been analyzed
- Improved spectroscopic parameters for the water vapor continuum and lines in the far-infrared and submillimeter regions have been derived
- The improved far-infrared spectroscopic parameters have a notable impact on calculated spectral radiances and a modest impact on broadband radiative fluxes and heating rates

Supporting Information:
- Supporting Information S1

Correspondence to:
E. J. Mlawer,
emlawer@aer.com

Citation:
Mlawer, E. J., Turner, D. D., Paine, S. N., Palchetti, L., Bianchini, G., Payne, V. H., et al. (2019). Analysis of water vapor absorption in the far-infrared and submillimeter regions using surface radiometric measurements from extremely dry locations. *Journal of Geophysical Research: Atmospheres*, *124*, 8134–8160. https://doi.org/10.1029/2018JD029508

Received 17 AUG 2018
Accepted 17 APR 2019
Accepted article online 2 MAY 2019
Published online 22 JUL 2019

Author Contributions:
Conceptualization: E. J. Mlawer, D. D. Turner
Data curation: D. D. Turner, R. L. Pernak
Formal analysis: E. J. Mlawer, D. D. Turner, S. N. Paine
Funding acquisition: E. J. Mlawer, D. D. Turner, S. N. Paine, L. Palchetti, M. G. Mlynczak
Investigation: E. J. Mlawer, D. D. Turner, S. N. Paine, L. Palchetti, G. Bianchini, J. S. Delamere, M. G. Mlynczak
(continued)

©2019. American Geophysical Union. All Rights Reserved.

Analysis of Water Vapor Absorption in the Far-Infrared and Submillimeter Regions Using Surface Radiometric Measurements From Extremely Dry Locations

E. J. Mlawer[1], D. D. Turner[2], S. N. Paine[3], L. Palchetti[4], G. Bianchini[4], V. H. Payne[5], K. E. Cady-Pereira[1], R. L. Pernak[1], M. J. Alvarado[1], D. Gombos[1,6], J. S. Delamere[1,7], M. G. Mlynczak[8], and J. C. Mast[9,10]

[1]Atmospheric and Environmental Research, Lexington, MA, USA, [2]NOAA/Earth System Research Laboratory/Global Systems Division, Boulder, CO, USA, [3]Smithsonian Astrophysical Observatory, Cambridge, MA, USA, [4]Istituto Nazionale di Ottica, Consiglio Nazionale delle Ricerche, Sesto Fiorentino, Italy, [5]Jet Propulsion Laboratory, NASA, California Institute of Technology, Pasadena, CA, USA, [6]Now at Morse Corp, Cambridge, MA, USA, [7]Now at Alpenglow Scientific, Fairbanks, AK, USA, [8]NASA Langley Research Center, Hampton, VA, USA, [9]Science Systems and Applications Inc., Hampton, VA, USA, [10]Now at Department of Atmospheric Sciences, Texas A&M University, College Station, TX, USA

Abstract The second Radiative Heating in Underexplored Bands Campaign (RHUBC-II) was conducted in 2009 by the U.S. Department of Energy Atmospheric Radiation Measurement program to improve water vapor spectroscopy in the far-infrared spectral region. RHUBC-II was located in an extremely dry region of Chile to ensure very low opacities in this spectral region. Spectrally resolved measurements by a far-infrared spectrometer and a submillimeter interferometer from RHUBC-II are compared with line-by-line radiative transfer model calculations. Water vapor amounts and temperatures used in the calculations come from collocated radiosondes, with extensive adjustments to correct for issues due to the campaign's dry conditions and mountainous terrain. A reanalysis is also performed of far-infrared measurements taken at the Atmospheric Radiation Measurement North Slope of Alaska site before and during the first RHUBC campaign. These analyses determine that differences between the measurements and model calculations using existing spectroscopic parameters are significant in the far-infrared and submillimeter regions, leading to the derivation of improved water vapor continuum absorption coefficients and air-broadened widths of 74 water vapor lines. The foreign continuum is increased by more than 50% in part of the far-infrared and the widths of more than 20 lines are changed by more than 10%. The uncertainty in the foreign continuum coefficients is estimated as greater than 20% in some spectral regions, primarily a consequence of the uncertainty in the specification of water vapor. The improved far-infrared spectroscopic parameters have a notable impact on calculated spectral radiances and a modest impact on broadband radiative fluxes and heating rates.

1. Introduction

Emission and absorption of thermal radiation by the atmosphere and surface are key processes that drive our weather and climate. Thermal radiative processes need to be represented accurately in atmospheric models for there to be confidence in these models' simulations. Our knowledge of gaseous absorption properties has a strong foundation in most of the longwave spectral region, where thermal radiative processes are dominant. Through a combination of theoretical spectroscopic calculations and laboratory and field radiometric observations, spectroscopic parameters have been derived and subsequently utilized by detailed line-by-line radiative transfer models in radiative closure studies that have in turn led to further refinements in these parameters (see, e.g., Mlawer & Turner, 2016). In this part of the spectrum, fast radiative transfer codes built from these line-by-line models can be used confidently for weather and climate prediction and remote sensing applications. However, in the far-infrared (far-IR, 100–600 cm^{-1}) and submillimeter (sub-mm, 10–100 cm^{-1}) regions of the longwave, the foundation of our knowledge is not nearly as strong, despite this region's important contribution to the total thermal energy in our atmosphere (Figure 1; Harries et al., 2008). (Note: The far-IR is sometimes defined as spanning 10–600 cm^{-1}; however, as the 10–100 cm^{-1} region contributes only a small amount to the surface or top-of-atmosphere energy budgets, here we define the far-IR to be only the 100- to 600-cm^{-1} region.)

Methodology: E. J. Mlawer, D. D. Turner, S. N. Paine, V. H. Payne, K. E. Cady-Pereira, J. S. Delamere, M. G. Mlynczak, J. C. Mast
Project administration: E. J. Mlawer, D. D. Turner
Software: D. D. Turner, S. N. Paine, V. H. Payne, R. L. Pernak, D. Gombos, J. S. Delamere, J. C. Mast
Supervision: E. J. Mlawer
Validation: E. J. Mlawer
Visualization: E. J. Mlawer, D. D. Turner, S. N. Paine, R. L. Pernak
Writing - original draft: E. J. Mlawer, D. D. Turner, S. N. Paine
Writing – review & editing: E. J. Mlawer, D. D. Turner, S. N. Paine, L. Palchetti, M. J. Alvarado

The significant far-IR contribution to the thermal energetics of the atmosphere and the dominant role of water vapor absorption in the far-IR demonstrate that solid knowledge of water vapor absorption properties in the far-IR is important for accurate analysis of key issues related to Earth's radiative balance and climate. This absorption consists of both water vapor lines and the underlying water vapor continuum. Remote sensing in both the far-IR and sub-mm also depend on accurate values for spectroscopic parameters in these spectral regions. However, due to the lack of sensitivity of surface downwelling far-IR radiation to these parameters under typical atmospheric conditions (green curves in Figures 2 and 3), far-IR radiative closure studies have been challenging to undertake. Another factor thwarting such studies was the lack, until recently, of instruments that make spectrally resolved radiometric measurements in the far-IR and sub-mm.

In the late 1990s, a far-IR radiative closure study (Tobin et al., 1999) that was performed as part of the Surface Heat Budget of the Arctic Ocean experiment led to important improvements to foreign-broadened continuum absorption coefficient values in the far-IR, but only a portion (400–600 cm^{-1}) of the far-IR was analyzed due to the limited spectral range of the instrument. After this analysis, the uncertainty of the key spectroscopic parameters of water vapor in the far-IR, even from 400–600 cm^{-1}, remained unacceptably high. With this motivation, the Atmospheric Radiation Measurement (ARM) Program (Ackerman & Stokes, 2003; Stokes & Schwartz, 1994; Turner & Ellingson, 2016) of the U.S. Department of Energy organized two field experiments, the Radiative Heating in Underexplored Bands Campaigns (RHUBC), to assess and improve our understanding of water vapor spectroscopy throughout the far-IR (Turner & Mlawer, 2010). The first RHUBC was held in 2007 at the ARM North Slope of Alaska (NSA) site in Utqiagvik (formerly Barrow; Verlinde et al., 2016) and resulted in significant improvements in our knowledge of the foreign continuum between 400 and 600 cm^{-1} and the widths of many absorption lines in this region (Delamere et al., 2010). The subsequent RHUBC-II campaign was held in 2009 at an elevated site on Cerro Toco in the Atacama Desert of Chile. During RHUBC-II, the precipitable water vapor (PWV) values were as much as 5 times lower than those encountered during RHUBC-I, allowing sensitivity to spectroscopic values throughout most of the far-IR and a large portion of the sub-mm spectral region. We report herein on our analysis of the observations taken during RHUBC-II, which has led to significant modifications to the water vapor foreign continuum and notable changes to water vapor foreign-broadened line widths and the self-continuum.

Since the two RHUBC campaigns were completed, other studies have used field observations to derive foreign continuum coefficients in the far-IR. Liuzzi et al. (2014) analyzed measurements from a far-IR spectrometer (same as utilized in RHUBC-II) that was deployed in a 2-year field campaign at Dome C in Antarctica. This analysis made use of the line widths determined in Delamere et al. (2010) and simultaneously retrieved foreign continuum coefficients in a large portion of the far-IR and the water vapor and temperature profiles used as input to the radiative transfer calculations. The methodology used in Liuzzi et al. (2014) improved upon an analysis performed on prior measurements from the same instrument as part of the Earth Cooling by Water Vapour Radiation campaign in Italy (Serio et al., 2008). Green et al. (2012) derived far-IR foreign continuum coefficients from measurements from an aircraft-based spectrometer over a range of water vapor amounts, undertaken as part of the Continuum Absorption by Visible and Infrared radiation and its Atmospheric Relevance initiative. The instrument used in that study was also deployed in RHUBC-I, but instrumental issues during the campaign thwarted the attainment of significant useable spectra (Fox et al., 2015). Finally, Shi et al. (2016) derived foreign continuum coefficients from 190–350 cm^{-1} from measurements by a Fourier transform spectrometer (FTS) configured for unattended operation and calibration that was deployed to the Chinese Kunlun research station at Antarctica Dome A. The results from these studies are discussed below.

After a brief recap of RHUBC-I, section 2 provides relevant information about the RHUBC-II campaign. Section 3 details the components of the radiative closure analysis for both RHUBC-II and the reanalysis of the RHUBC-I data set: the radiometric measurements, the radiative transfer models, and the specification of the atmospheric state used needed for the calculations. (Further details about the instruments and the specification of the atmospheric state can be found in the supporting information). Section 4 provides the results of the comparisons between the measurements and calculations for RHUBC-II (far-IR and sub-mm) and RHUBC-I (far-IR), most notably the modifications made to the water vapor continuum and line widths needed to attain radiative closure. A validation is also performed using an independent far-IR

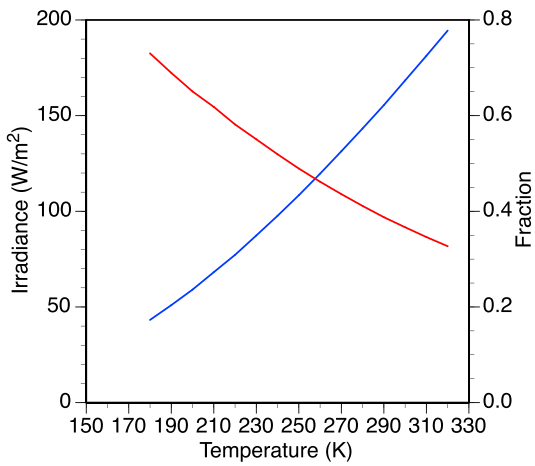

Figure 1. Plotted with respect to the blackbody temperature, (blue, left axis) the total integrated thermal irradiance in the far-infrared and submillimeter regions (10–600 cm^{-1}) and (red, right axis) its fraction with respect to the total broadband thermal irradiance.

measurement data set from RHUBC-II, and comparisons are made with other studies of the far-IR foreign continuum. Section 5 details the impact of these spectroscopic improvements on calculated fluxes and heating rates. The final section summarizes both RHUBC campaigns and the need for further studies of water vapor spectroscopy in the far-IR.

2. The RHUBC Campaigns

2.1. RHUBC-I

The RHUBC-I campaign was held at the ARM NSA site in Utqiagvik, Alaska, over 3 weeks in the winter of 2007. Clear and cold conditions characterized this period, ideal for achieving the main objective of the campaign, the evaluation and improvement of water vapor spectroscopic parameters in the far-IR. Details about the RHUBC-I experiment and analysis can be found in Delamere et al. (2010), which is the reference for the basic information provided in this subsection (unless otherwise noted).

In addition to the usual instrumental suite present at NSA, including the Atmospheric Emitted Radiance Interferometer-Extended Range (Knuteson et al., 2004a, 2004b; AERI-ER; more detail on the AERI is provided below), during RHUBC-I the site hosted a number of guest instruments targeted at the campaign's objectives. A second far-IR radiometric instrument, the Tropospheric Airborne FTS (TAFTS; Canas et al., 1997), a FTS operating from 80–600 cm^{-1} with a spectral resolution of 0.12 cm^{-1} was also present for RHUBC-I. In addition to the standard ARM 183 GHz microwave radiometer (Cadeddu et al., 2007), essential for specifying the water vapor column above the site, two other microwave radiometers were present, and an analysis demonstrated that these instruments agreed well with each other (Cimini et al., 2009). In addition, the usual twice-a-day radiosonde launches were augmented by 48 additional sondes over the campaign's duration. As expected, dry conditions prevailed, with numerous occurrences of PWV values near 1.0 mm. The range of PWV (see Figure 3 of Turner & Mlawer, 2010) was 0.9–2.4 mm.

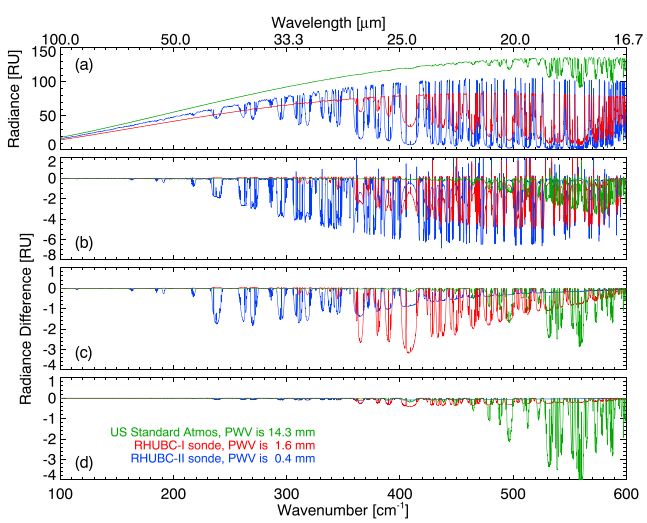

Figure 2. (a) Calculated downwelling radiance in the far-infrared for the U.S. Standard Atmosphere (green) and for typical radiosondes from the RHUBC-I (red) and RHUBC-II (blue) campaigns. The change in the downwelling radiance if (b) the water vapor air-broadened line widths are increased by 20%; (c) the foreign continuum is increased by 20%; and (d) the self-continuum is increased by 20%. A "radiance unit" (RU) is 1 mW/(m^2·sr·cm^{-1}). RHUBC = Radiative Heating in Underexplored Bands Campaign; PWV = precipitable water vapor.

Accurate specification of the water vapor profile in the column above a ground-based radiometric instrument is of critical importance in a radiative closure study that is focused on absorption due to water vapor (Revercomb et al., 2003; Turner et al., 2004). In RHUBC-I, the water vapor abundances measured by the sondes were scaled to agree with the PWV retrieved from one of the 183 GHz radiometers, resulting in an PWV uncertainty of ~2% (Cimini et al., 2009; Delamere et al., 2010). With these profiles as input to the radiative transfer model, comparisons between model calculations and AERI-ER measurements demonstrated significant disagreement, and, as a result, modifications were made to the water vapor continuum and the widths of 42 strong water vapor lines between 400 and 600 cm^{-1}. These changes had significant impact on computed atmospheric radiative fluxes and were shown to contribute to small but statistically significant changes to temperature, humidity, and cloud fields in a 20-year climate simulation (Turner, Merrelli, et al., 2012).

Despite the success of RHUBC-I in improving our knowledge of far-IR water vapor spectroscopy, a major portion of the far-IR remained "underexplored" after this campaign. Two factors prevented RHUBC-I from extending its results below 400 cm^{-1}. First, the PWV values during the campaign were not low enough to provide much sensitivity to spectroscopic parameters for wavenumbers less than 400 cm^{-1} (red curves in Figure 2). Second, instrumental issues plagued the TAFTS during RHUBC-I, resulting in this instrument collecting only a very limited number of valid spectra (Fox et al., 2015). To allow for further progress, a second RHUBC campaign was organized and undertaken.

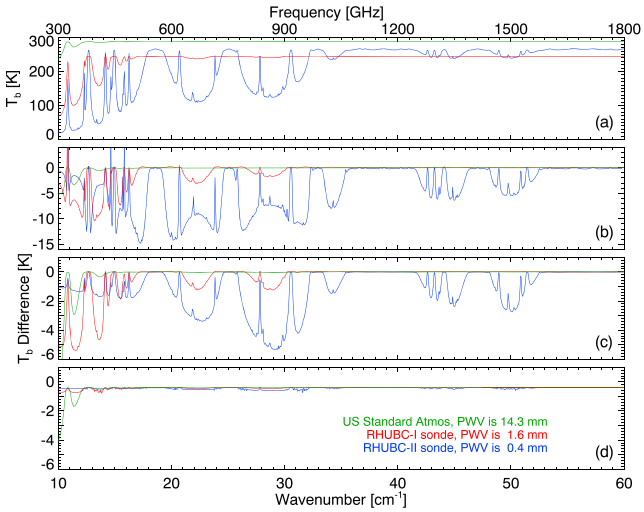

Figure 3. The same as Figure 2, but for the submillimeter with the radiance values expressed in brightness temperature. The 60- to 100-cm^{-1} region is not shown since in this region the change in brightness temperature with respect to changes in widths and the foreign and self-continua are very small.

2.2. RHUBC-II

The Atacama Desert of northern Chile is well known for its clear and dry conditions (e.g., Rutllant Costa, 1977) and, for that reason, has been chosen to host a number of astronomical observatories. This includes the Atacama Large Millimeter/submillimeter Array, an array of 66 antennas situated at ~5,000-m elevation in the Chajnantor Plateau in the Atacama. The combination of the ideal climatic conditions plus the advanced infrastructure developed in this region due to the presence of Atacama Large Millimeter/submillimeter Array led ARM to hold the second RHUBC campaign on the upper slopes of a mountain, Cerro Toco, that borders this plateau. Based on climatological analysis, RHUBC-II was held during the late winter/early spring (August–October of 2009) to maximize the chances of cloud-free periods characterized by very low PWV values.

The high altitude (5,380 m) and remote location of RHUBC-II presented a number of challenges. The site was an hour's drive, much over unpaved mountain roads, from accommodations (at 2500 m elevation), so safety and health concerns led to an approximate "every-other-day" operations schedule, with an operational day limited to 4–5 hr in the morning. No operations were held at night. Many of the instruments needed to be deployed manually each day, so remote data acquisition was not possible. The micropulse lidar (Campbell et al., 2002) that was first installed at the site to identify clouds did not function properly, and a replacement lidar was not able to be shipped and set up until late in the campaign. Despite these and other challenges, a wealth of valuable radiometric measurements were acquired during the campaign by five different instruments (section 3), with other measurements providing contemporaneous information on the atmospheric state relevant to radiative transfer. Additional information about RHUBC-II can be found in Turner and Mlawer (2010) and Turner, Mlawer, et al. (2012).

The particular challenges of the RHUBC-II deployment necessitated use of a different approach to specify the atmospheric state than that of previous similar closure studies (e.g., Delamere et al., 2010; Turner et al., 2004). Westerly winds of 20–30 m/s were persistent, immediately whipping the Vaisala RS92-k radiosondes horizontally after launch. Within 20 m, they had passed over a large cliff and into the leeward wake of the mountain. (see Figure 9 in Marín et al., 2013, for RHUBC-II site orography.) Therefore, not only were sondes measuring atmospheric conditions not over the radiometric instrument, their recorded pressure and temperature values were for an elevation above ground hundreds of meters greater than its elevation over the site and influenced by mountainous terrain. These factors made the radiosonde measurements far less representative of the radiating column than in previous closure studies and, as described below, led to alternate approaches to specify these critical atmospheric state parameters.

3. Components of the Radiative Closure Study

A radiative closure experiment is a comparison between radiometric measurements and the calculations of a radiative transfer model that utilizes a best guess of the atmospheric (and, possibly, surface) properties required for the calculation. The quality of each of the three components in the experiment—the measurements, the radiation code, and the specification of the atmospheric state—is of critical importance in ensuring that the conclusions of the study advance our understanding of the processes being examined. This section details the elements of the RHUBC-II closure study.

3.1. Radiometric Measurements

Six instruments making spectrally resolved radiation measurements were deployed to the Cerro Toco site for RHUBC-II. Two instruments provided measurements throughout the far-IR, the Radiation Explorer in the Far-Infrared-Prototype for Applications and Development (REFIR-PAD; Palchetti et al., 2005, 2008) and the Far-Infrared Spectroscopy of the Troposphere (FIRST; Mlynczak et al., 2006). Closure analysis related to the REFIR-PAD measurements is presented in this paper (section 4.1.1), and this analysis is validated

using FIRST observations (section 4.2). (A complete analysis of the RHUBC-II FIRST measurements is the focus of Mast et al., 2017.) We also present here (section 4.1.3) the results of a radiative closure analysis using measurements in the sub-mm region by the Smithsonian Astrophysical Observatory submillimeter FTS (SAO-FTS; Paine et al., 2000; Paine & Turner, 2013) during this campaign. Measurements from two other radiometric instruments deployed in RHUBC-II were used in this study to specify important atmospheric state parameters used in the radiative transfer model calculations. IR measurements from the AERI (Knuteson et al., 2004a, 2004b) were used to derive temperature values for the lower atmosphere (section 3.2.3 and the supporting information). Also, microwave measurements from the G-band Water Vapor Radiometer Profiler (GVRP; Cimini et al., 2009), which was one of the three radiometers providing measurements on the 183.3-GHz water vapor line during RHUBC-I, provided information on RHUBC-II water vapor profiles (section 3.2.3 and the supporting information). The shortwave instrument, the Absolute Solar Transmittance Interferometer (Hawat et al., 2002), which was deployed to make spectral measurements from 2,000–10,000 cm^{-1} (1–5 μm), did not function well during the campaign and its measurements are not used in the analysis presented here.

The presence of these instruments in one location, which spanned the entire thermal longwave region, resulted in what we believe is the first-ever high spectral resolution observation of the entire thermally emitted spectrum, an example of which was shown in Figure 2 of Turner, Mlawer, et al. (2012).

Details on the design and calibration of the key radiometric instruments used in RHUBC-II, the REFIR-PAD, SAO-FTS, GVRP, and AERI, can be found in the supporting information of this manuscript. Detailed information about the FIRST instrument (spectral range 100–1,000 cm^{-1}, nominal resolution 0.643 cm^{-1}) and its deployment in RHUBC-II is in Mast et al. (2017).

3.2. Line-by-Line Radiative Transfer Calculations

3.2.1. Radiative Transfer Models

LBLRTM. LBLRTM (available at rtweb.aer.com; Clough et al., 2005) is an accurate and flexible radiative transfer model that can be used over the full spectral range from the microwave to the ultraviolet and has had a long and successful heritage at the leading edge of the field. Radiative closure studies performed with ARM data (Mlawer & Turner, 2016) have been crucial in establishing LBLRTM as a state-of-the-science radiative transfer model. LBLRTM has been used in ground-based retrieval schemes (Turner & Blumberg, 2018; Turner & Löhnert, 2014), to develop radiation codes such as RRTMG for climate applications (Iacono et al., 2000; Mlawer et al., 1997; Mlawer et al., 2016), to train forward models utilized in operational satellite retrievals (Clerbaux et al., 2007; Clough et al., 2006) and data assimilation schemes (e.g., the Community Radiative Transfer Model; Liu & Boukabara, 2014), and to provide reference calculations for model intercomparison studies (Oreopoulos et al., 2012; Pincus et al., 2015). The breadth and importance of these applications attests to the role that LBLRTM has played and continues to play in advancing atmospheric and climate science.

MonoRTM. MonoRTM (available at rtweb.aer.com; Clough et al., 2005; Payne et al., 2011) is a radiative transfer model that utilizes the same physics as LBLRTM but is designed to process a limited number of monochromatic spectral output values with higher accuracy. MonoRTM is commonly utilized in the microwave spectral region and also is appropriate for use for laser propagation studies in other spectral domains.

The *am* program (available at http://doi.org/10.5281/zenodo.1193771; Paine, 2017) is a radiative transfer code developed for modeling the terrestrial atmosphere in radio astronomy and remote sensing applications at microwave through sub-mm wavelengths. Its principal strengths are numerical efficiency, ease of integration with other software, and flexible modeling of spectrometers and receiver systems. Recent versions of *am* explicitly track the water vapor line and continuum spectroscopy in the AER radiative transfer codes.

3.2.2. Spectroscopic Parameters

As in Delamere et al. (2010), the main objective of this study is the evaluation of current water vapor spectroscopic parameters (line widths and continuum) based on the observations taken during the campaign and, if necessary, adjustments to these parameters to improve the agreement between the radiometric measurements and the radiation calculations. This section details the line parameters and continuum version used as baseline parameters for this study and places those values in the context of the results of Delamere et al. (2010).

Table 1
Definitions of the Combinations of Line Width and Continuum Versions Referred to in This Study

Label	Line widths	Continuum
Pre-RII	aer_v_3.4.1	MT_CKD_2.8
Pre-RII_HIT	HITRAN 2012	MT_CKD_2.8
Post-RII	aer_v_3.5	MT_CKD_3.0

The three radiative transfer models used in this study evaluate the optical depth contributions of each line out to ± 25 cm^{-1} from its center and consider any contribution further from the line center as part of the continuum. For LBLRTM, the Voigt profile (symmetrized as in Van Vleck & Huber, 1977; see also Clough et al., 1989) is utilized and computed with an algorithm based on a linear combination of approximating functions (for species like CO_2, CH_4, and O_2, these functions are modified to account for line mixing). In MonoRTM, the Humlicek (1972) algorithm is used to compute the symmetrized Voigt line shape for all pressure regimes (also adjusted for line mixing, if present). For *am*, line shapes are specified by species and model layer. For the sub-mm analysis, given the low-frequency and wide instrumental resolution, Doppler broadening is negligible and default pressure-broadened line shapes are used in the *am* models for this study. In particular, the default water vapor line shape is Van Vleck-Huber with the ±25-cm^{-1} line wing cutoff noted above. In addition to the line contributions, all three of these models utilize the MT_CKD water vapor continuum model (Mlawer et al., 2012), which conceptually can be understood as including contributions from all water vapor lines further than 25 cm^{-1} from their centers plus any line contributions within 25 cm^{-1} not consistent with the Voigt line shape. The MT_CKD water vapor continuum was initially formulated as the sum over all water vapor lines of a single line shape fitted to maximize agreement with continuum measurements available at the time of its creation (see Mlawer et al., 2012, for more details), but subsequently, the MT_CKD absorption coefficients have been modified in certain spectral regions based on more recent analyses of laboratory and atmospheric spectra.

The analysis of radiative transfer model calculations that utilize different combinations of spectroscopic parameters provides the foundation for this study. Since we will be referring to these combinations throughout this manuscript, we define labels for each of these combinations in Table 1.

Water vapor absorption lines. The intensities and positions of water vapor lines used in Delamere et al. (2010) for the RHUBC-I analysis were from calculations by Coudert et al. (2008) based on both measurements and a theoretical model. These values were used for the calculations designated "LBL09" in Delamere et al. (2010) and were incorporated in the line parameter database (i.e., linefile) AER_v_2.2. The group that performed these spectroscopic calculations subsequently provided updated intensities that were incorporated into HITRAN 2012 below 800 cm^{-1} for lines with intensities greater than 10^{-26} $cm^{-1}/(molecule/cm^2)$ (Rothman et al., 2013). These intensities were adopted in the linefile AER_v_3.4.1 (and its successor, AER_v_3.5, that is derived in the current study) and are used for all LBLRTM calculations presented here. The ratio of the HITRAN 2012 water vapor line intensities to those in AER_v_2.2 are shown in Figure 4 for the spectral region of interest. Somewhat larger intensity differences than these have been shown to result in only a small change in calculated radiances (see Figures 7 and 8c in Delamere et al., 2010).

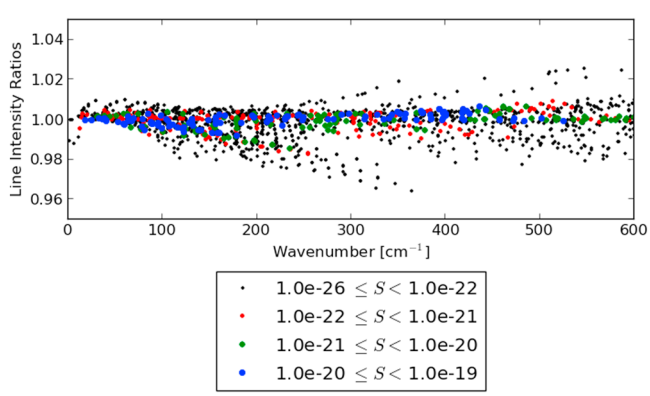

Figure 4. Ratios of water vapor line intensities in HITRAN 2012 (same as AER_v_3.4.1 and AER_v_3.5) to those in AER_v_2.2 color-coded by line intensity ($cm^{-1}/[molecule/cm^2]$).

A major result of Delamere et al. (2010) was the determination of air-broadened widths for 42 far-IR water vapor transitions between 400 and 600 cm^{-1} that improved upon the width values in the 2006 HITRAN water vapor update file. These width improvements were incorporated into the AER_v_2.2 linefile and were also in AER_v_3.4.1. As was the case for the 2006 HITRAN update, the HITRAN 2012 database utilizes the procedure described in Gordon et al. (2007) to determine air-broadened widths of water vapor lines, although the width values changed between HITRAN 2006 and 2012 due to updated data being input to the procedure. However, this input did not include the widths determined in Delamere et al. (2010). For far-IR lines not analyzed in Delamere et al. (2010), AER_v_3.4.1 adopted the widths from the HITRAN 2008 database (Rothman et al., 2009). The ratios of the widths in HITRAN 2012 to those in AER_v_3.4.1 are shown in the center panel of Figure 5.

Figures 6b and 6c show the residuals between the REFIR-PAD measurements and LBLRTM calculations using widths from AER_v_3.4.1

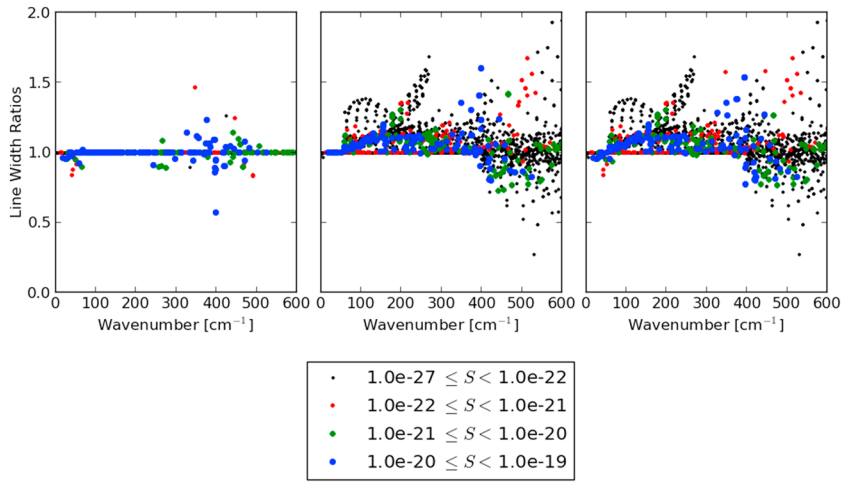

Figure 5. Ratios of air-broadened widths of water vapor transitions color-coded by line intensity (cm^{-1} /[molecule/cm^2]): (left) ratios of AER_v_3.4.1 (same as Delamere et al., 2010, for wavenumbers > 400 cm^{-1}) to AER_v_3.5; (center) ratios of HITRAN 2012 to AER_v_3.4.1; and (right) ratios of HITRAN 2012 to AER_v_3.5.

(labeled "Pre-RII"; see Table 1) and HITRAN 2012 (labeled "pre-RII_HIT"), respectively, for all RHUBC-II cases with PWV between 0.3 and 0.5 mm. All other spectroscopic values, including the water vapor continuum coefficients, are the same for these two sets of calculations, as are the input profiles. (The construction of the input profiles will be described below.) Not surprisingly, the residuals above 400 cm^{-1} for the PRE-RII calculations (AER_v_3.4.1) are smaller than for PRE-RII_HIT, reflecting the width improvements in Delamere et al. (2010) that were not incorporated into HITRAN 2012. Below 400 cm^{-1}, both sets of widths result in significant residuals, with AER_v_3.4.1 being generally better than HITRAN 2012 above 300 cm^{-1} and worse at lower wavenumbers. Based on these results, the baseline widths used in this study were from AER_v_3.4.1.

Water vapor continuum. The MT_CKD foreign and self-continua in the far-IR have undergone a number of modifications since the generation of MT_CKD_1.0 (Mlawer et al., 2012). Although this initial version of MT_CKD took into account the far-IR continuum coefficients determined by Tobin et al. (1999), a subsequent reassessment of the agreement between the coefficients and MT_CKD_1.0 led to a modification of the far-IR foreign continuum, released as MT_CKD_1.2. This continuum version provided the baseline for the Delamere et al. (2010) study, which used ARM NSA AERI-ER measurements from 400–600 cm^{-1} to improve the MT_CKD_1.2 foreign continuum. Improvements to the MT_CKD_1.2 foreign and self-continuum coefficients in the microwave were also derived by Payne et al. (2011). These microwave self-continuum adjustments were modeled as extending to higher wavenumbers, so the continuum version presented in Delamere et al. (2010), MT_CKD_2.4, had modifications to both the foreign and self-continuum coefficients in the far-IR. In the far-IR, MT_CKD_2.4 is identical to MT_CKD_2.8, which is utilized as the benchmark version for this study. Figure 7 demonstrates the differences between the foreign continuum in MT_CKD_2.4 and its predecessors. All these versions, however, share a key element: all continuum coefficients between 10 and 400 cm^{-1} come from fits that interpolate between the observationally determined values in the microwave (<6 cm^{-1}) and above 400 cm^{-1}. The continuum in this gap, in the radiatively potent, but underexplored, spectral region between 10 and 400 cm^{-1}, is analyzed in this study, allowing most of this region to be filled in with values derived from observations.

Other spectroscopic parameters. Since the tail of the CO_2 ν_2 band impacts the high wavenumber end of the far-IR region, we provide here some information on this band's implementation in LBLRTM, which is the same for all versions analyzed in this study. All CO_2 line parameters needed for the Voigt line shape have been obtained from the HITRAN 2012 database with the adjustments made by Lamouroux et al. (2015). For CO_2, the Voigt function needs to be modified to account for line mixing to accurately compute the sub-Lorentzian behavior in the band wings. The first order approximation to line mixing, which is used for CO_2 lines in LBLRTM, is based on an expansion in terms of pressure of the full line mixing equation (Hartmann et al., 2008) and assumes that the first two terms of the expansion (the Voigt line shape plus

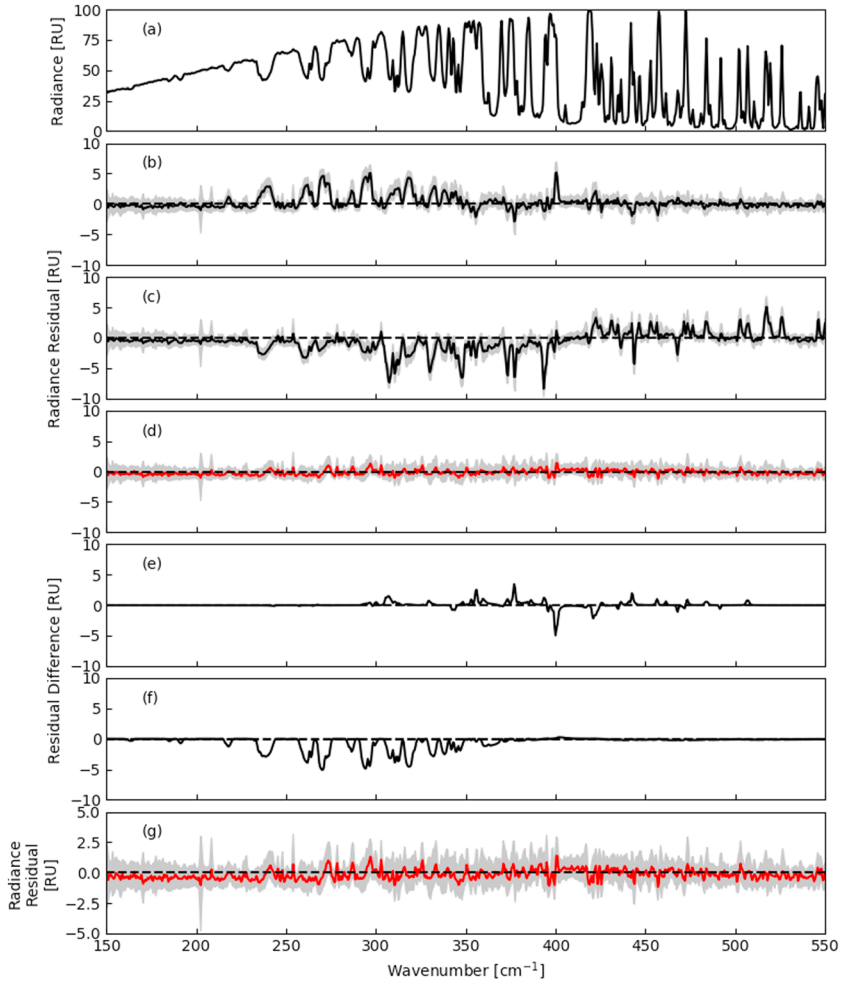

Figure 6. RHUBC-II REFIR-PAD results from 150–550 cm^{-1} for 117 cases with 0.3 mm < PWV < 0.5 mm. (a) Median REFIR-PAD radiances; (b) median residuals between REFIR-PAD and LBLRTM using Pre-RII; (c) median residuals between REFIR-PAD and LBLRTM using Pre-RII_HIT; (d) median residuals between REFIR-PAD and LBLRTM using Post-RII (i.e., after the improvements presented in this work); (e) change in residuals between Post-RII and Pre-RII due to the change in widths; (f) change in residuals between Post-RII and Pre-RII due to the change to the water vapor continuum; and (g) same results as shown in panel d, but with scale expanded to enable residual features to be viewed more easily. Gray envelopes in panels b–d and g show the interquartile range of the residuals. The random noise of the REFIR-PAD in the laboratory is about 1 RU. RHUBC = Radiative Heating in Underexplored Bands Campaign; PWV = precipitable water vapor; REFIR-PAD = Radiation Explorer in the Far-Infrared-Prototype for Applications and Development.

an asymmetric correction term) accurately describe the effect of line mixing on the line shape. The implementation of this approximation that is used in LBLRTM is based on Lamouroux et al. (2015), which, in turn, is based on the Niro et al. (2005) approach to P-, Q-, and R-branch line mixing for CO_2.

3.2.3. Input to the RHUBC-II Calculations

A brief overview of the approach used to determine the atmospheric profiles input to the radiative transfer calculations performed in this study is provided in this section. Figure 8 provides a schematic depiction of this approach. A more detailed description is also given in the supporting information.

In brief, numerous modifications are made to the sonde-measured water vapor and temperature profiles, many of which try to overcome the issue that the RHUBC-II sondes did not accurately represent the atmospheric properties in the column above the radiometric instruments. First, an adjustment is made to the sonde water vapor profiles to correct for known biases in low humidity conditions (Miloshevich et al., 2009). A continuous sounding product, referred to as "TI-sounding" (similar to that described in Troyan, 2012), is created, and then certain of its components are modified as follows:

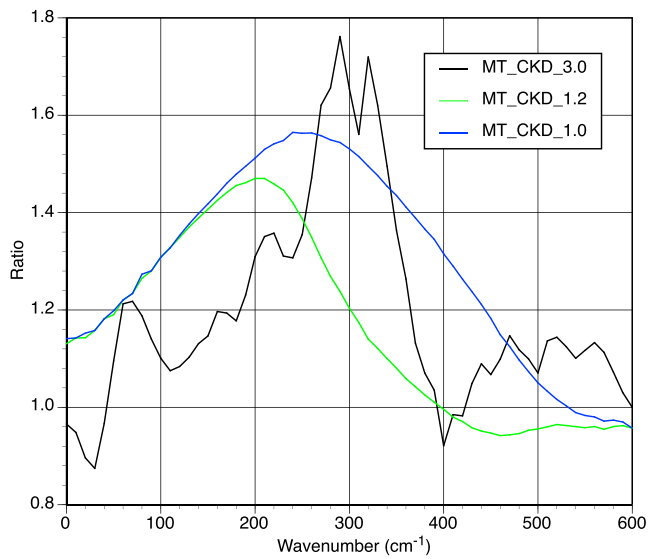

Figure 7. Ratios of water vapor foreign continuum values from different versions of MT_CKD with respect to MT_CKD_2.8 (same as MT_CKD_2.4). Values are plotted every 10 cm^{-1}.

1. Temperature profiles in the lowest 3,000 m are replaced by profiles retrieved using AERI measurements in the 15- and 4.3-μm carbon dioxide bands
2. Water vapor profiles are replaced by profiles retrieved from GVRP measurements (i.e., on the 183-GHz line in microwave).

Since the responsivity of the AERI steadily decreased throughout the campaign (see section S.1.4), AERI temperature retrievals were not performed after 24 September 2009 and no cases analyzed in this paper are from after that date. From this modified sounding product (termed "RETR-sounding"), two versions of a final set of profiles are created. First, based on an analysis of residuals between LBLRTM calculations that use RETR-sounding and REFIR-PAD measurements from 400–550 cm^{-1}, all water vapor profiles in RETR-sounding are scaled by 7%. This version of the profiles is used in the far-IR REFIR-PAD analysis. The second version of the profiles is created by performing a PWV scale factor retrieval for each SAO-FTS spectra analyzed. This version is used in the SAO-FTS analysis.

It is important to note that the adjustments made to TI-sounding that are based on retrievals using radiometric measurements (hexagons in Figure 8) are primarily performed in spectral regions in which we have more confidence in our spectroscopic knowledge than we have in the spectroscopy that we target in this study:

1. Uncertainties are low for the spectroscopic parameters of the IR carbon dioxide bands, which are widely used for temperature retrievals from satellite observations.
2. The properties of the 183-GHz water vapor line and corresponding water vapor continuum also have modest uncertainties (Cimini et al., 2018; Payne et al., 2008; Payne et al., 2011) and measurements on this line have been relied upon in previous similar studies (e.g., Delamere et al., 2010).
3. Water vapor line parameters and continuum from 400–550 cm^{-1} have been analyzed in Delamere et al. (2010) and improvements implemented, allowing this study to utilize this region with some confidence.

In this study, there is one exception to the practice of implementing profile adjustments only if the measurements on which these adjustments are based are in spectral regions with spectroscopic parameters that have previously been investigated in some detail, which is our use of SAO-FTS measurements to constrain the PWV for our sub-mm analysis. To assess the degree of circularity that this approach might create, this retrieval is performed both using the original spectroscopy and the revised spectroscopy that is derived in the current study (section 4.1.3). Since the two sets of scale factors are effectively equivalent (e.g., median scale factors differ by 0.3% for cases with PWV between 0.3 and 0.5 mm), we conclude that this adjustment to the profiles is sufficiently independent of the derived spectroscopy.

4. Measurement-Calculation Comparisons

In this section, radiative closure analyses using RHUBC-II measurements are presented. Analyses covering the 10- to 600-cm^{-1} spectral region are split into different spectral regions since the analysis in each region involves a distinct set of measurements.

4.1. Radiative Closure Analyses

4.1.1. RHUBC-II Far-IR Analysis (200–405 cm^{-1})

The REFIR-PAD measurements from RHUBC-II are grouped into subsets based on PWV. Due to the high variability of the residuals between the measurements and LBLRTM calculations, the analysis focuses on the only PWV subset that consists of a sufficiently large number of cases, 0.3 mm < PWV < 0.5 mm (see Table 2). After a few cases are removed from this data set due to issues with spectral calibration, this subset consists of 117 cases. (All REFIR-PAD results presented hereafter are for this subset.) For this PWV range, as shown by the blue curve in Figure 2, semitransparent microwindows are present in the far-IR even below 240 cm^{-1}. As discussed above, the residuals corresponding to the baseline calculations of LBLRTM (Pre-RII, i.e., the far-IR water vapor continuum and widths after Delamere et al., 2010), shown in Figure 6b, are

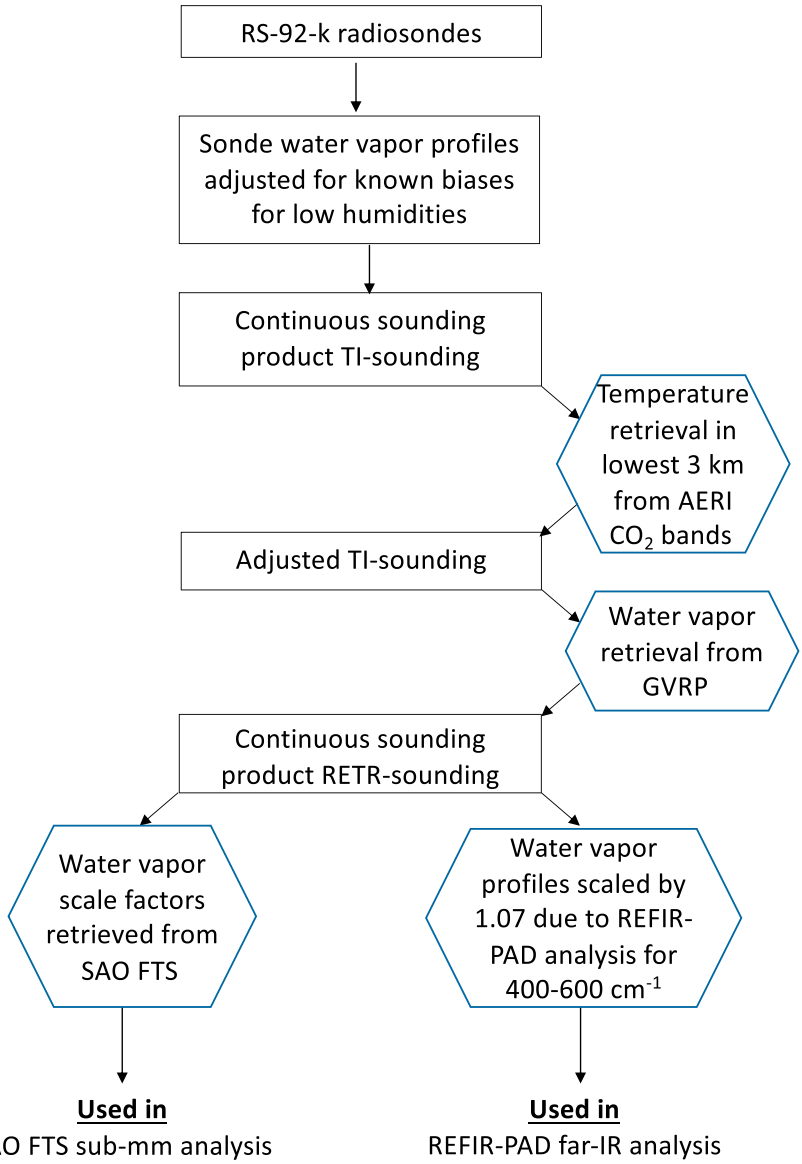

Figure 8. Schematic description of the construction of the temperature and water vapor profiles used in this study. SAO-FTS = Smithsonian Astrophysical Observatory submillimeter Fourier transform spectrometer; AERI = Atmospheric Emitted Radiance Interferometer; GVRG-band Water Vapor Radiometer Profiler.

Table 2
Number of Cases in Each PWV Bin in the REFIR-PAD and SAO-FTS Data Sets Used in This Analysis

		REFIR-PAD		SAO-FTS	
Bin	PWV range	Number	Number	Median PWV scale factor	IQR of PWV scale factors
1	<0.3 mm	33	114	0.971	0.099
2	0.3–0.5 mm	117	132	0.995	0.101
3	0.5–0.8 mm	21	45	0.964	0.070
4	>0.8 mm	6	13	0.952	0.277

Note. All cases are from on or before 24 September 2009 (see section 3.2.3 and the supporting information). For the SAO-FTS analysis, also shown are the median PWV ($H_2{}^{16}O$) scale factors (relative to baseline scale factor of 1.05; see supporting information section) and interquartile range for all PWV bins.

significant throughout the 200- to 405-cm^{-1} spectral region, deviating from zero at numerous spectral locations by more than their respective interquartile ranges. A comparison of Figures 6a and 6b indicates that significant residuals occur both on the wings of strong water vapor absorption lines, where the optical depth is primarily due to these lines, and in microwindows between lines, where the relative contribution of the foreign continuum is substantial.

Based on these results, adjustments are made to the air-broadened widths of a number of strong water vapor lines between 240 and 405 cm^{-1}. These modified widths are adopted in the AER_v_3.5 linefile and are listed in Table 3, along with the respective widths in AER_v_3.4.1 and HITRAN 2012, and the ratios of the new widths to the previous values. These ratios are also shown in the left and right panels of Figure 5, color coded by line intensity. Table 3 also provides the uncertainty ranges provided in HITRAN 2012 (Rothman et al., 2013) for the widths in that database. Most of the width changes are less than 20%, although a few are somewhat larger, and more than half fall outside the listed uncertainty range of the HITRAN 2012 widths. Some of these adjusted widths are for lines that are close neighbors of other strong water vapor absorption lines. Since the impacts of these lines overlap, the widths determined by this analysis should be considered as effective widths, derived to obtain optimal agreement with the REFIR-PAD measurements. We cannot rule out that other sets of width changes would also lead to approximately equivalent radiative closure. In Table 3, we provide an estimate for the width uncertainty only for each line that is sufficiently strong and isolated from other lines (i.e., no strong line within 1 cm^{-1} on at least one side of the line center) to allow an unadulterated determination of its width. In these cases, the width uncertainty is estimated at 7% or, in cases in which the derived width agrees more closely than 7% with the AER_v_3.4.1 width, the percentage given by the ratio of the two widths. (As described below, widths of absorption lines in other regions of the far-IR and in the sub-mm were also modified in this study, and appear in Table 3 and Figure 5.)

In addition, modifications were also made to the foreign continuum in this region to improve the measurement-calculation agreement. The changes are discussed below (section 4.2), after the results from other instruments and spectral regions are presented.

The improved residuals from 200–405 cm^{-1} as a result of the spectroscopic modifications (label "Post-RII"; see Table 1) in this region can be seen in Figure 6d. Both the magnitude of the median spectral residuals and their variability are much lower than with the spectroscopic parameters used in panels b and c, and the median residual for each spectral point is well within the interquartile range of that point's residuals for the cases in the data set. The contributions to the change in the residuals (equal to minus the change in calculated radiances) due to the width and continuum modifications are shown in panels e and f, respectively.

4.1.2. Reanalysis of NSA AERI-ER Measurements (> 400 cm^{-1})

Due to the extremely dry conditions that characterized RHUBC-II, the REFIR-PAD measurements are relatively insensitive to water vapor spectroscopic parameters above 400 cm^{-1}, with the only exception being in the immediate vicinity of strong lines. Therefore, the AERI-ER data set from NSA analyzed in Delamere et al. (2010) is a better foundation for the determination of water vapor spectroscopic parameters above 400 cm^{-1}, with the RHUBC-II REFIR-PAD data set able to only provide supporting information. Figure 6c of that previous work shows the spectral residuals after all modifications to line widths and continuum absorption were made. (Note that the AERI-ER measures down to 400 cm^{-1}, while the AERI instrument that was deployed for RHUBC-II does not provide useful measurements below 520 cm^{-1}.)

There are a number of compelling arguments to reanalyze the NSA AERI-ER data set in the current study. First, recent changes in water vapor line intensities (>400 cm^{-1} in Figure 4) would modify the previous model calculations in this region, spoiling the radiative closure that resulted from the previous analysis. Second, the final spectral residuals obtained in Delamere et al. (2010) left room for improvement. Third, the RHUBC-II REFIR-PAD measurements from 395–405 cm^{-1} provide a perspective on the cluster of strong lines in that region that could not be provided by the AERI-ER, which did not measure below 400 cm^{-1}, thereby raising questions about the spectroscopic adjustments made previously in that small spectral region. The final reason to reanalyze the NSA AERI-ER data set is that recent changes to microwave spectroscopy (Birk & Wagner, 2012; Ma et al., 2010; Rothman et al., 2013) imply that the water vapor profiles used in the original analysis, which depended on measurement-model comparisons near the 183-GHz absorption line, no longer could be considered best guess profiles. The PWV retrievals in Delamere et al. (2010) utilized air-broadened half-widths described in Payne et al. (2008) and continuum (equivalent to MT_CKD_2.4)

Table 3
Line Positions, Intensities, and Air-Broadened Widths of Lines With Widths That Were Modified in This Study

Wavenumber (cm^{-1})	Line intensity (cm^{-1}/[molecule/cm^2])	Widths: AER_v_3.5 (cm^{-1})	Widths: AER_v_3.4.1 (cm^{-1})	Widths: HITRAN 2012 (cm^{-1})	Width ratios: AER_v_3.5/AER_v_3.4.1	Width ratios: AER_v_3.5/HITRAN 2012
H_2O lines						
18.577	5.207E−20	0.1103[a]	0.1060	0.1060[d]	1.041	1.041
20.704	5.685E−22	0.0876	0.0834	0.0834[d]	1.050	1.050
25.085	3.433E−20	0.1072[a]	0.1022	0.1022[c]	1.049	1.049
30.560	1.423E−21	0.0960[a]	0.0912	0.0912[d]	1.053	1.053
32.954	2.498E−20	0.1045[a]	0.1006	0.1006[c]	1.039	1.039
40.988	4.766E−20	0.1040[a]	0.1009	0.1009[b]	1.031	1.031
42.638	7.212E−22	0.0905	0.0756	0.0756[d]	1.197	1.197
43.244	7.012E−22	0.0970	0.0846	0.0846[d]	1.147	1.147
44.099	5.712E−21	0.0875	0.0859	0.0859[d]	1.019	1.019
47.053	1.402E−19	0.0965[a]	0.0997	0.0997[c]	0.968	0.968
48.059	9.418E−22	0.0890	0.0854	0.0854[d]	1.042	1.042
51.434	1.532E−21	0.0900	0.0853	0.0853[d]	1.055	1.055
52.511	2.314E−22	0.0880	0.0801	0.0801[d]	1.099	1.099
59.947	4.777E−20	0.0970	0.0894	0.0924[d]	1.085	1.050
67.246	8.013E−21	0.0970	0.0869	0.0907[d]	1.116	1.069
68.063	7.257E−20	0.0880[a]	0.0893	0.0914[d]	0.985	0.963
244.207	5.974E−20	0.0685	0.0621	0.0685[d]	1.103	1.000
257.100	8.273E−21	0.0571	0.0510	0.0572[d]	1.120	0.998
265.139	2.909E−21	0.0420	0.0377	0.0426[d]	1.114	0.986
267.560	8.737E−21	0.0240	0.0259	0.0284[d]	0.927	0.845
275.376	2.366E−21	0.0800	0.0708	0.0782[d]	1.130	1.023
298.417	3.845E−20	0.0780	0.0741	0.0783[d]	1.053	0.996
302.982	8.584E−19	0.0395	0.0404	0.0510[d]	0.978	0.775
302.985	2.861E−19	0.0395	0.0404	0.0510[d]	0.978	0.775
303.111	6.034E−19	0.0500	0.0592	0.0670[d]	0.845	0.746
328.168	9.412E−20	0.0520[a]	0.0592	0.0668[d]	0.878	0.778
334.155	8.408E−23	0.0350	0.0313	0.0366[d]	1.118	0.956
343.205	3.631E−20	0.0750[a]	0.0705	0.0771[d]	1.064	0.973
348.464	4.588E−22	0.0500	0.0733	0.0787[d]	0.682	0.635
351.995	7.144E−20	0.0460[a]	0.0511	0.0580[d]	0.900	0.793
354.119	1.006E−19	0.0750	0.0804	0.0821[d]	0.933	0.914
354.589	1.146E−19	0.0561	0.0641	0.0665[d]	0.875	0.844
357.267	7.231E−20	0.0800[a]	0.0880	0.0877[d]	0.909	0.912
369.998	3.807E−20	0.0800[a]	0.0785	0.0784[d]	1.019	1.020
374.496	1.343E−19	0.0376	0.0393	0.0478[d]	0.957	0.787
374.501	4.479E−20	0.0346	0.0367	0.0477[d]	0.943	0.725
376.216	8.840E−20	0.0420[a]	0.0516	0.0579[d]	0.814	0.725
378.546	1.424E−21	0.0750	0.0724	0.0728[d]	1.036	1.030
384.838	2.764E−20	0.0780	0.0827	0.0837[d]	0.943	0.932
385.503	1.261E−20	0.0895	0.0927	0.0905[d]	0.965	0.989
394.229	7.265E−20	0.0256	0.0279	0.0392[d]	0.918	0.653
394.229	2.421E−20	0.0256	0.0279	0.0392[d]	0.918	0.653
396.433	2.399E−20	0.0910[a]	0.0807	0.0808[d]	1.128	1.126
397.319	5.853E−20	0.0740	0.0804	0.0815[c]	0.920	0.908
397.676	3.154E−20	0.0660	0.0565	0.0508[c]	1.168	1.299
398.941	1.843E−20	0.0440	0.0415	0.0510[d]	1.060	0.863
398.976	5.531E−20	0.0440	0.0414	0.0509[d]	1.063	0.864
400.222	1.068E−20	0.0700	0.0400	0.0639[c]	1.750	1.095
400.481	1.067E−20	0.0400	0.0350	0.0408[b]	1.143	0.980
419.872	6.700E−20	0.0770[a]	0.0693	0.0660[c]	1.111	1.167
422.962	2.011E−20	0.0465[a]	0.0420	0.0369[c]	1.107	1.260
423.617	9.876E−23	0.0600	0.0759	0.0760[d]	0.791	0.789
425.327	1.016E−20	0.0490[a]	0.0507	0.0403[b]	0.966	1.216
426.294	1.314E−21	0.0850[a]	0.0876	0.0870[d]	0.970	0.977
434.805	2.633E−21	0.0680[a]	0.0630	0.0522[d]	1.079	1.303
436.426	4.681E−21	0.0201	0.0209	0.0220[e]	0.962	0.914
436.426	1.404E−20	0.0201	0.0209	0.0220[e]	0.962	0.914

Table 3
(continued)

Wavenumber (cm^{-1})	Line intensity (cm^{-1}/[molecule/cm^2])	Widths: AER_v_3.5 (cm^{-1})	Widths: AER_v_3.4.1 (cm^{-1})	Widths: HITRAN 2012 (cm^{-1})	Width ratios: AER_v_3.5/AER_v_3.4.1	Width ratios: AER_v_3.5/HITRAN 2012
441.714	3.619E−21	0.0850	0.0819	0.0851[d]	1.038	0.999
442.088	9.823E−21	0.0835	0.0952	0.0690[b]	0.877	1.210
443.696	1.073E−20	0.0365	0.0373	0.0462[d]	0.979	0.790
443.701	3.575E−21	0.0365	0.0373	0.0461[d]	0.979	0.792
447.415	2.044E−22	0.0450	0.0560	0.0710[d]	0.804	0.634
456.873	4.944E−21	0.0830[a]	0.0909	0.0667[c]	0.913	1.244
461.450	5.033E−21	0.0240	0.0254	0.0226[c]	0.945	1.062
461.450	1.677E−21	0.0240	0.0254	0.0226[c]	0.945	1.062
467.893	1.148E−21	0.0375	0.0335	0.0473[d]	1.119	0.793
467.920	3.446E−21	0.0375	0.0334	0.0473[d]	1.123	0.793
470.507	6.119E−22	0.0450	0.0411	0.0489[d]	1.095	0.920
472.168	1.136E−20	0.0650	0.0609	0.0527[c]	1.067	1.233
472.757	1.646E−20	0.0750	0.0804	0.0698[c]	0.933	1.074
483.985	1.013E−20	0.0825[a]	0.0850	0.0727[b]	0.971	1.135
491.606	9.816E−22	0.0420	0.0351	0.0468[d]	1.197	0.897
491.716	3.274E−22	0.0420	0.0349	0.0466[d]	1.203	0.901
506.924	9.013E−21	0.0750[a]	0.0783	0.0666[b]	0.958	1.126
O_2 lines						
27.824	1.365E−25	0.0521[a]	0.0496	0.0496[c]	1.050	1.050
48.927	5.212E−25	0.0499[a]	0.0475	0.0475[c]	1.051	1.051
50.872	1.555E−25	0.0499	0.0475	0.0475[c]	1.051	1.051

Note. For O_2 lines, self-broadened widths were modified by the same factor as listed.
[a]Uncertainty is the lesser of 7% and the percentage that corresponds to the AER_v_3.5/AER_v_3.4.1 ratio. [b]Uncertainty range provided in HITRAN 2012: 1–2%. [c]Uncertainty range provided in HITRAN 2012: 2–5%. [d]Uncertainty range provided in HITRAN 2012: 5–10%. [e]Uncertainty range provided in HITRAN 2012: 10–20%.

from the analysis of Payne et al. (2011). The air-broadened line width of the 183-GHz line derived in Payne et al. (2008) assumed certain values of the temperature dependence of the air-width and of the self-broadened half-width. More recent versions of the HITRAN compilation (Rothman et al., 2013) contain updated values for these parameters, so the Payne et al. (2008) 183-GHz air-broadened width needs reconsideration. The temperature dependence of the air-width (0.68) in HITRAN 2012 is based on measurements (Birk & Wagner, 2012) of the line with the same rotational quantum numbers in a different water vapor absorption band (ν_2 band). Updated calculations specifically for the 183-GHz line suggest a value of 0.71 (Ma et al., 2010), which is still within the range of uncertainty of the HITRAN 2012 value. We adopt this value for the temperature dependence and the self-broadened width from the HITRAN 2012 compilation and repeat the width analysis of Payne et al. (2008) with the same set of ground-based measurements to derive a value of 0.1025 $cm^{-1}\cdot atm^{-1}$ for the air-width. All microwave spectroscopic parameters related to the analysis of the NSA data set are summarized in Table 4.

Using this set of revised parameters for the 183-GHz line, the water vapor profiles for our reanalysis of the NSA AERI-ER data set are obtained by scaling the profiles used in Delamere et al. (2010) so that the calculated brightness temperatures at 183 ± 7 GHz equals the brightness temperatures obtained with the parameters and water vapor profiles used in the earlier analysis. This results in profiles that have an average PWV 0.9% higher (standard deviation 0.1%) than the original values—this small increase attests to the low spectroscopic uncertainty associated with this line. Using these scaled profiles, LBLRTM calculations from 400–600 cm^{-1} are performed with this study's baseline spectroscopy (Pre-RII), which includes the widths determined in the earlier study, for the 17 cases analyzed in that work. The residuals from these runs can be seen in Figure 9b, and exceed the interquartile range of the residuals in a number of spectral locations. Based on both our reanalysis of the NSA AERI-ER cases and consideration of the RHUBC-II REFIR-PAD measurements, modifications to line widths and continuum are determined in this region. As can be seen in Figure 9d, these modifications (Post-RII) lead to discernible improvements to the AERI-ER residuals. Table 3 includes the line widths in this region that were modified in this study—some of the

Table 4
Microwave Spectroscopic Parameters Used in the Analysis

Spectroscopic parameters		Payne et al. (2008)	Delamere et al. (2010)	HITRAN 2012	This work
183 GHz	Air width $(cm^{-1}\ mol\ cm^{-2})^{-1}$	0.0997	0.0997	0.0992	0.1025
	Self-width $(cm^{-1}\ mol\ cm^{-2})^{-1}$	0.449	0.449	0.519	0.519
	T exponent	0.77	0.77	0.68	0.71
	P shift $(cm^{-1}\ mol\ cm^{-2})^{-1}$	−0.00269	−0.00269	−0.00270	−0.00270
Continuum version		CKD_2.4	MT_CKD_2.4 (equiv)	—	MT_CKD_2.5.2
MonoRTM version		v3.3	v4.2	—	v5.2

widths modified in Delamere et al. (2010) are modified here and some are unchanged, while widths have also been changed for lines not on the original list. These width changes can also be seen in Figure 5a.

The continuum changes in this region will be discussed further below.

Comparing Figures 6b (Pre-RII) and 6d (Post-RII) for 395–550 cm^{-1} shows that these width and continuum modifications also have a positive impact on REFIR-PAD residuals near strong lines. In particular, the

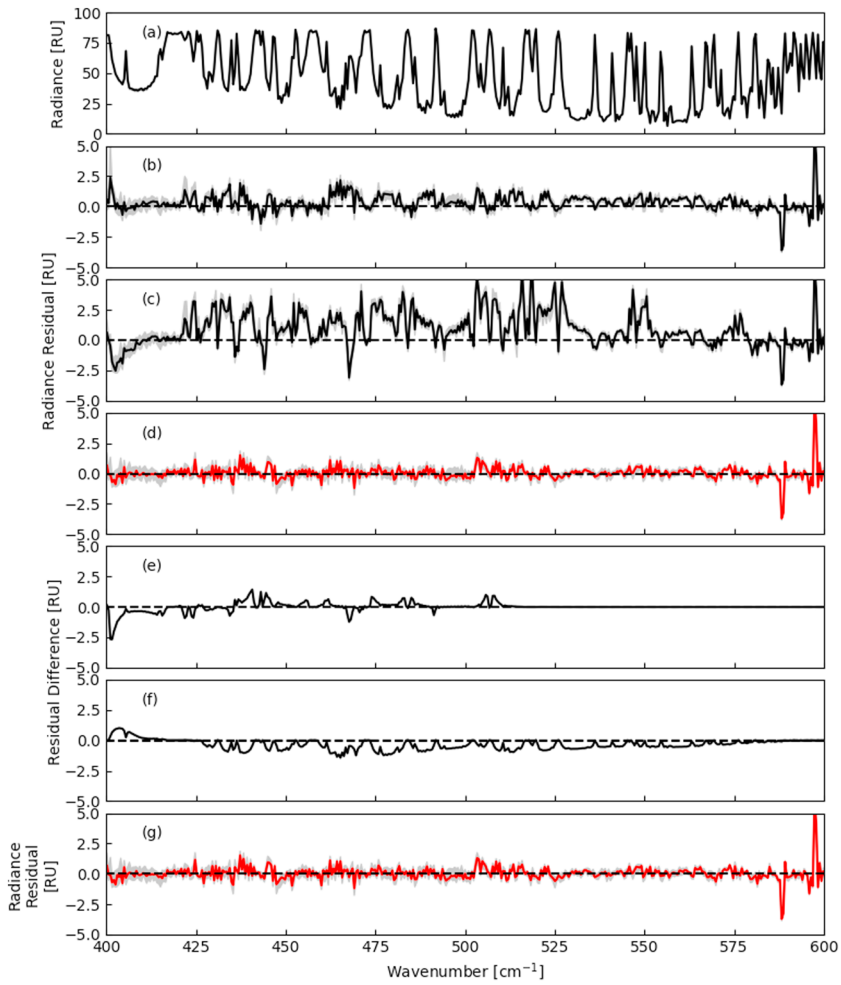

Figure 9. North Slope of Alaska AERI-ER analysis from 400–600 cm^{-1} for the 17 cases from Delamere et al. (2010). (a) Median AERI-ER radiances; (b) median residuals between AERI-ER and LBLRTM using Pre-RII (same water vapor line widths derived in Delamere et al., 2010); (c) median residuals between AERI-ER and LBLRTM using Pre-RII_HIT; (d) median residuals between AERI-ER and LBLRTM using Post-RII (i.e., after the improvements presented in this work); (e) change in residuals between Post-RII and Pre-RII due to the change in widths; and (f) change in residuals between Post-RII and Pre-RII due to the change to the water vapor continuum. Gray envelopes in panels b–d show the interquartile range of the residuals. AERI-ER = Atmospheric Emitted Radiance Interferometer-Extended Range.

improved residuals between 395 and 405 cm^{-1} for the REFIR-PAD (as well as for the AERI-ER data set) belie the speculation in Delamere et al. (2010) that there is unmodeled line coupling of water vapor lines within this group of lines.

4.1.3. SAO-FTS Analysis (15–60 cm^{-1})

During RHUBC-II, sub-mm spectra were produced at 10-min intervals by the SAO-FTS. This instrument acquired one-sided interferograms, so that the total power and low-resolution calibration of the spectra were dominated by the data taken toward the beginning of a scan. For this reason, each retrieved water vapor and temperature profile used in the radiative closure analysis was paired with the SAO-FTS spectrum for which the start of the FTS scan was closest in time, provided that the start-of-scan time stamp is within 10 min of the retrieved profile time stamp. Following this scheme, from one to three vertical profiles in RETR-sounding are associated with each acquired spectrum. Each of these profiles is subsequently modified, both to scale the PWV to better match the associated measurement and to account for a small small water vapor absorption layer within the instrument. The details of these adjustments are provided in the supporting information.

It is interesting to note that the median PWV scale factors obtained by the procedure described in the supporting information are quite consistent for all PWV bins, as shown in Table 2. When this procedure is repeated using TI-sounding profiles (used as the prior in the GVRP retrieval) instead of RETR-sounding profiles, the resulting PWV scale factors are much less consistent, ranging from 0.923 (bin1) to 1.217 (bins 3 and 4). (These values are applied on top of a 0.80 scaling that is needed to center the range for linearization.) The consistency in Table 2 attests to the additional information about the profile contributed by the GVRP.

For each profile, a model Planck brightness temperature spectrum T_b is computed using the *am* code, and spectral residuals are computed with respect to the associated measured T_b spectrum from the SAO-FTS. Like the REFIR-PAD spectra, the SAO-FTS spectra and residuals are binned by PWV range. The two driest bins, designated bin 1 (PWV < 0.3 mm, 114 cases) and bin 2 (0.3 mm ≤ PWV < 0.5 mm, 132 cases) are used in the sub-mm analysis. The median brightness temperature spectrum for each of these bins is plotted in Figure 10a.

The bin 1 and bin 2 analyses indicate that the widths in Pre-RII of a number of water vapor and oxygen lines need modification. As shown in Table 3 and Figure 5, we adjust the widths of 16 water vapor and 3 oxygen lines. The water vapor foreign continuum is also adjusted to reduce the residuals in microwindows in the sub-mm region for bin 1 and bin 2 cases (discussed further below). To demonstrate the impact of these spectroscopic changes, the retrieval process described above is run with the original and modified spectroscopic parameters. Figure 10 shows that the improvement in the spectral T_b residuals is significant, and largely consistent, in both the bin 1 and bin 2 cases. Figures 10b and 10c are computed using Pre-RII (AER_v_3.4.1 and MT_CKD_2.8) and Pre-RII_HIT (HITRAN 2012 and MT_CKD_2.8), respectively. Panel d shows the improved residuals using Post-RII (AER_v_3.5 and MT_CKD_3.0; discussed in next section). For bin 2, a similar comparison is shown in panels e, f, and g. Finally, to clarify the spectral shape of the changes associated with these adjustments, panel h shows the change in residuals associated only with the line width changes from AER_v_3.4.1 to AER_v_3.5, holding the continuum constant at MT_CKD_3.0, and panel i shows the effect of changing the continuum from MT_CKD_2.8 to MT_CKD_3.0, holding the line parameters constant at AER_v_3.5.

We also note that the sub-mm HDO scale factors that are derived using the revised H_2O spectroscopy (obtained as described in the supporting information) indicate that the driest cases are the most HDO-depleted, as expected. When the HDO scale factors are derived using the previous H_2O spectroscopic parameters, the relationship between HDO depletion and PWV is the reverse of the expected fractionation.

4.2. Implications for the Water Vapor Continuum

As discussed above, radiative closure analyses performed with observations from the RHUBC-II REFIR-PAD and SAO-FTS, and with the NSA AERI-ER (most cases from RHUBC-I) lead to the modification of the widths of many water vapor lines in the far-IR and sub-mm regions and three oxygen lines in the sub-mm. The modified widths have been included in the AER_v_3.5 linefile. The widths of these lines, as well as the corresponding values in existing spectroscopic databases are provided in Table 3.

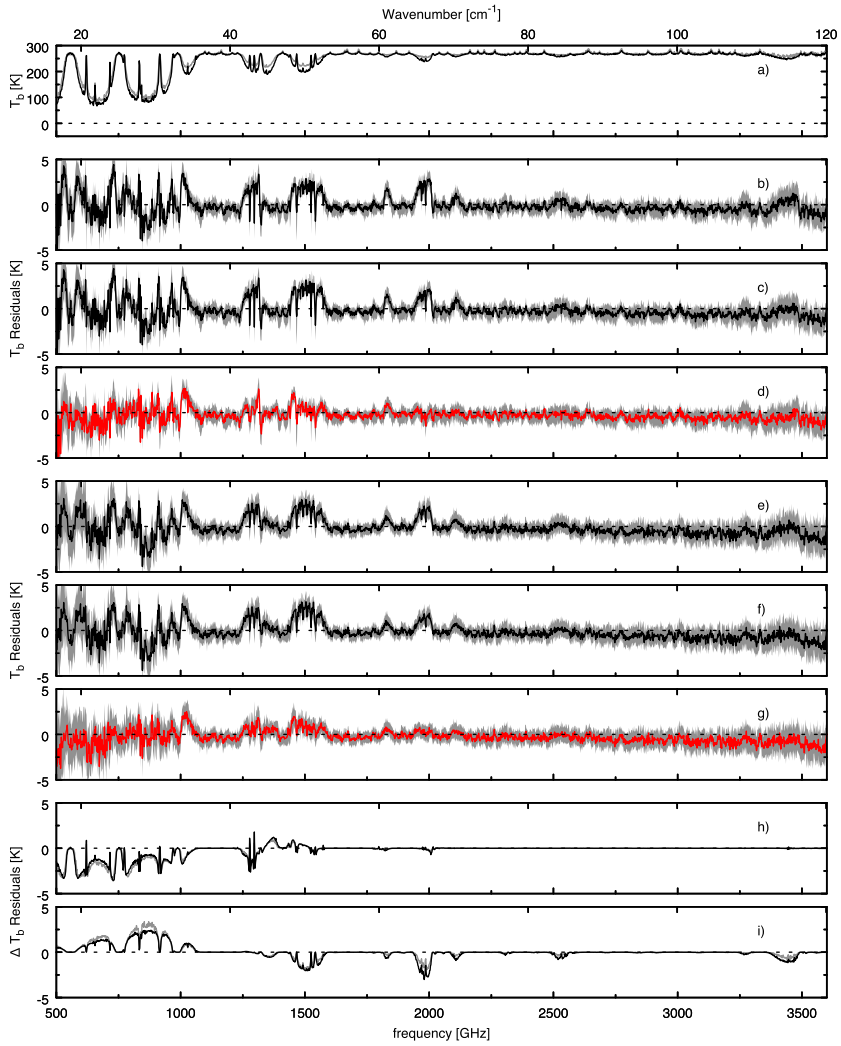

Figure 10. Analysis of Smithsonian Astrophysical Observatory submillimeter Fourier transform spectrometer measurements from Radiative Heating in Underexplored Bands Campaign-II. (a) Median measured brightness temperatures (T_b) from 500–3,600 GHz (17–120 cm^{-1}) for cases with PWVs < 0.3 mm (bin1, black) and 0.3 mm < PWV < 0.5 mm (bin2, gray); (b) median bin1 T_b residuals for *am* calculations using Pre-RII; (c) median bin1 T_b residuals with pre-RII_HIT; (d) median bin1 T_b residuals with Post-RII; (e) median bin2 T_b residuals for *am* calculations with Pre-RII; (f) median bin2 T_b residuals with Pre-RII_HIT; (g) median bin2 T_b residuals with Post-RII; (h) change in residuals between Post-RII and Pre-RII due to the change in widths (same colors as in panel a); and (i) change in residuals between Post-RII and Pre-RII due to the change to the water vapor continuum. Gray envelopes in panels b–g show the interquartile range of the residuals. PWV = precipitable water vapor.

The closure analyses also indicate that the MT_CKD_2.4 (same as MT_CKD_2.8) water vapor foreign continuum in the far-IR and sub-mm regions needs revision. In most of the 400- to 600-cm^{-1} spectral region analyzed in Delamere et al. (2010), our reanalysis of the AERI-ER measurements results in a small increase in the foreign continuum (see black curve in Figure 7), although in the immediate vicinity of 400 cm^{-1} the previous continuum coefficients only require very minor modifications to attain radiative closure. From 250–400 cm^{-1}, a large increase in the foreign continuum is required to obtain agreement with the REFIR-PAD measurements. Below 250 cm^{-1}, even the spectral regions with lowest opacity have little sensitivity to continuum changes, although the limited information in these microwindows indicates that the existing foreign continuum needs to be increased by a smaller percentage than at wavenumbers above 250 cm^{-1}. From 15–60 cm^{-1}, the closure analysis with SAO-FTS measurements demonstrates that the foreign continuum needs to be decreased to obtain agreement. In the 100–400 cm^{-1} region, the foreign continuum modifications determined in this study go in the opposite direction of the foreign continuum changes

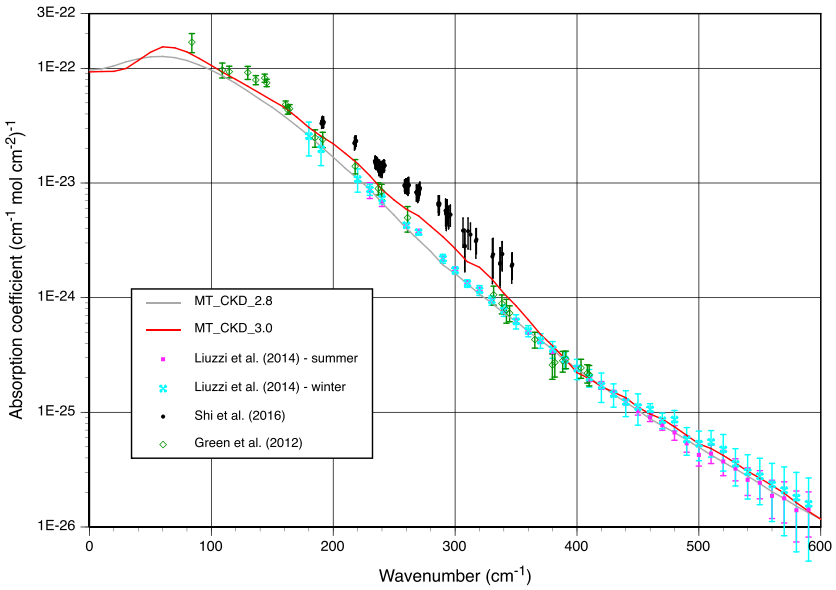

Figure 11. Water vapor foreign continuum coefficients in the far-infrared. The red and gray curves show MT_CKD_3.0 and MT_CKD_2.8, respectively. The symbols are coefficients derived by previous far-infrared studies.

implemented in MT_CKD_2.4 in Delamere et al. (2010). However, in this region, Delamere et al. (2010) inferred the continuum behavior from its measured values outside the 100- to 400-cm^{-1} region. The current study has been able to replace this inference with observational analysis across much of this region.

These foreign continuum modifications are implemented in MT_CKD_3.0, which is constructed to agree with the newly derived continuum coefficients in each region while maintaining smooth and continuous behavior, including interpolating across the observational "gap" between 60 and 200 cm^{-1} and transitioning above 600 cm^{-1} to the same values as in MT_CKD_2.8. For some spectral locations between 250 and 550 cm^{-1}, the construction of MT_CKD_3.0 prioritizes agreement with observations over smoothness, thereby leading to a degree of spikiness when compared with previous versions (Figure 7). However, the continuum coefficients themselves are still fairly smooth (Figure 11). The values of MT_CKD_3.0 at low wavenumbers (i.e., microwave, less than 15 cm^{-1}) require special consideration. The microwave foreign continuum coefficients in MT_CKD_2.8 follow from the analysis in Payne et al. (2011) of multiple data sets of microwave observations at a number of microwave frequencies, although the most definitive analysis was at 31.4 GHz. A smooth continuation of the SAO-FTS sub-mm analysis to lower frequencies suggests that the microwave foreign continuum coefficients determined in Payne et al. (2011) may be too high. We therefore repeat the analysis that led to Figure 8a in Payne et al. (2011) but with updated line parameters for the 22-GHz water vapor line. This revised analysis leads to a slight shift of the region of lowest cost function in Figure 8a of Payne et al. (2011) to the left (i.e., lower foreign continuum) and up (higher self-continuum). Therefore, for MT_CKD_3.0 the microwave foreign continuum is decreased by 3% from its previous value, allowing greater consistency with the analysis at the low-frequency end of the SAO-FTS. The MT_CKD_3.0 foreign continuum values for 0–600 cm^{-1} are shown in Figure 11.

The changes to the foreign continuum in the microwave necessitates compensating changes to the self-continuum to maintain consistency with the results of Payne et al. (2010). Therefore, the MT_CKD_3.0 self-continuum coefficients are increased slightly in this region (8% at 0 cm^{-1}, tailing off to less than 1% at 80 cm^{-1}).

The analysis of the FIRST measurements from RHUBC-II presented in Mast et al. (2017) concluded that no adjustments to the MT_CKD continuum could be justified given the combined uncertainties of all elements in the radiative closure study. In particular, the instrument calibration uncertainty of the FIRST and the uncertainty in the specification of the water vapor field were pointed to as concerns. The Mast et al. (2017) analysis indicated, however, that an increase in the foreign continuum in the far-IR would improve the agreement between FIRST observations and LBLRTM calculations. (It is worth noting that the Mast et al., 2017, study used an earlier version of the water vapor and temperature profiles used in the current study.)

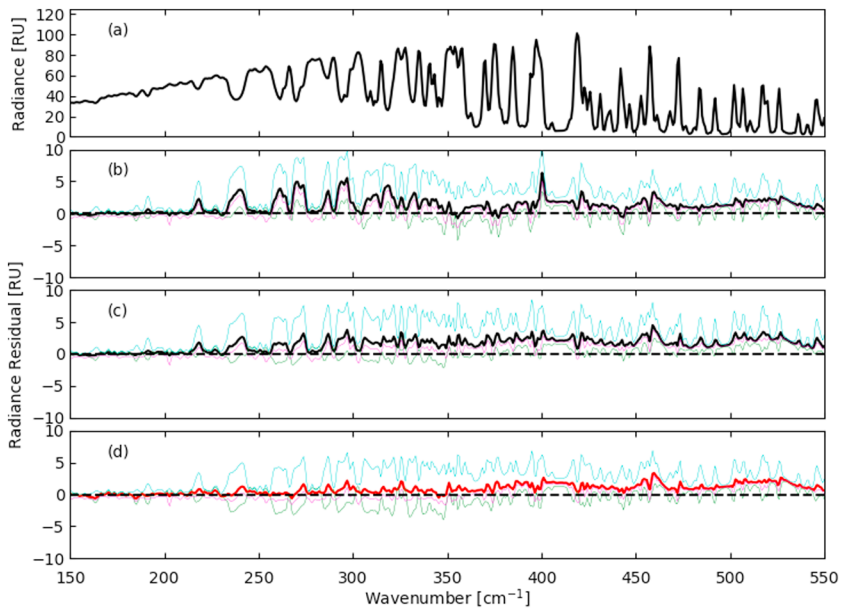

Figure 12. Radiative Heating in Underexplored Bands Campaign-II FIRST results from 150-550 cm^{-1} for cases A, B, and C from Mast et al. (2017). Precipitable water vapors = 0.32, 0.25, and 0.30 mm, respectively. (a) Mean FIRST radiances; (b) mean (black curve) and individual case (cyan, magenta, and green, respectively) residuals between FIRST and LBLRTM using Pre-RII spectroscopy and RETR-sounding profiles with water vapor scaled by 1.07; (c) mean and individual case residuals between FIRST and LBLRTM using Post-RII spectroscopy and RETR-sounding profiles; (d) mean (red) residuals between FIRST and LBLRTM using Post-RII spectroscopy and RETR-sounding profiles with water vapor scaled by 1.07. FIRST = Far-Infrared Spectroscopy of the Troposphere.

Here we use FIRST measurements to validate that the spectroscopic parameters derived in this study improve the agreement between observed and calculated radiances. This evaluation is limited to the three cases before 24 September 2009, that were analyzed in Mast et al. (2017). Unlike for the REFIR_PAD analysis above, the analysis of each FIRST case involves more than a single measurement scan and an LBLRTM calculation using one atmospheric profile. Instead, following Mast et al. (2017), a 35-min period is defined for each case and all FIRST scans and RETR_sounding profiles in that period are used. This results in an averaging of between 182-195 measurements and 8-12 LBLRTM calculations per case in the FIRST analysis presented here, helping to limit the large residual variances encountered in the REFIR_PAD comparisons. For the three cases, Figure 12 presents a comparison between the measurements and radiances calculated by LBLRTM using RETR-sounding atmospheric profiles with the water vapor scaled by 1.07. The calculations follow the same approach (e.g., instrument function, internal "hot path") as described in Mast et al. (2017). Panels b and d of Figure 12 show the results using Pre-RII and Post-RII spectroscopy, respectively. The improvement in agreement resulting from the new spectroscopic parameters is clear, especially for 230–400 cm^{-1}, and occurs both in spectral regions primarily sensitive to line widths and in microwindow regions, which are mostly sensitive to the continuum. Figure 12c shows the residuals with Post-RII spectroscopy when the 1.07 scaling is removed (i.e., using RETR-sounding). The magnitude of these residuals is greater than in Figure 12d, which substantiates the need for the water vapor scaling.

Figure 11 also demonstrates the relationship between the foreign continuum coefficients determined in this study to those derived in previous studies that included measurements below 400 cm^{-1}. Above 400 cm^{-1}, the MT_CKD_3.0 coefficients agree with the values from Liuzzi et al. (2014); listed as REFIR-L "summer" and "winter" in Figure 11, following the notation in Liuzzi et al., 2014) and Green et al. (2012), although MT_CKD_2.8 is also in agreement with the results of these studies given their provided uncertainties. The coefficients derived in the current study show better agreement than MT_CKD_2.8 with the drier winter cases in Liuzzi et al. (2014). Not shown in Figure 11 are the results of Sussmann et al. (2016), which determined foreign continuum coefficients between 400 and 600 cm^{-1}. The coefficients determined in that work agree better with MT_CKD_2.8 than MT_CKD_3.0, although the MT_CKD_3.0 and Sussmann et al. (2016) coefficients still generally agree in light of the uncertainties of the two continuum data sets. Between 350 and

400 cm^{-1}, all the coefficients plotted in Figure 11 agree better with the weaker MT_CKD_2.8 coefficients than they do with MT_CKD_3.0. Below 350 cm^{-1}, the studies tend to agree that MT_CKD_2.8 is too weak, although there are significant differences between them. While Liuzzi et al. (2014) is consistent with MT_CKD_2.8, the coefficients determined by Green et al. (2012) in this region are increasingly more consistent with MT_CKD_3.0 with decreasing wavenumber. The Shi et al. (2016) values are significantly higher than MT_CKD_3.0 and the other studies. In the vicinity of 100 cm^{-1}, the Green et al. (2012) measurements are somewhat greater than MT_CKD_3.0, which, in this region, follows an interpolated function that spans the spectral gap between 60 and 200 cm^{-1} in which the atmosphere was opaque in RHUBC-II despite the extremely low PWV values.

Following the recent release of MT_CKD_3.0 and the linefile AER_v_3.5, Rizzi et al. (2018) demonstrated excellent closure between LBLRTM calculations that used these parameters and REFIR-PAD measurements from Dome-C in Antarctica, demonstrating a significant improvement in radiative closure compared to the previous version of LBLRTM. That the Rizzi et al. (2018) study was performed on observations taken in an environment characterized by greatly different pressure and temperature profiles than encountered in RHUBC-II provides some confidence in the applicability of the spectroscopic parameters determined in the current study.

4.3. Uncertainty Analysis

A number of factors contribute to the uncertainty of the foreign continuum coefficients in the sub-mm region.

1. Uncertainty in the PWV scale factors in the SAO-FTS analysis (Table 2) leads to uncertainty in the continuum. The scale factor retrieval is most sensitive to the near wings of lines, so the residuals in continuum regions after the scaling is applied are a function of the accuracy of the line parameters. To evaluate this, we repeat the scale factor retrieval using different, but reasonable, water vapor air-broadened line widths than were used for the scale factor retrieval described above. In particular, we use the AER_3.4.1 widths in the alternate scale factor retrieval, which results in brightness temperature values in the continuum-dominated region (not shown) that differ from the previous calculations by an amount equivalent to an 8%, 6%, and 9% perturbation in the foreign continuum in the microwindows centered at 675 GHz (22.5 cm^{-1}), 850 GHz (28.3 cm^{-1}), and 1500 GHz (50 cm^{-1}), respectively. Since the line widths are the major, but not the only, source of line parameter uncertainty, we therefore slightly increase these values to estimate the continuum uncertainty from PWV uncertainty.
2. Uncertainty in the distribution of water vapor in the column also leads to uncertainty in the continuum due to the scaling with pressure of the foreign continuum. (The scaling of the line widths with pressure will also have a secondary effect on the continuum coefficients derived.) This uncertainty is assessed by repeating the SAO-FTS analysis using the TI-sounding profiles (priors in the GVRP retrieval) as the starting point for the PWV scale factor retrieval approach described above instead of the water vapor profiles retrieved using the GVRP observations (as described in section 3.2.3). Using the scale factors retrieved using this alternate set of water vapor profiles, *am* calculations are performed using Post-RII (AER_v_3.5 and MT_CKD_3.0). The differences (not shown) between the computed brightness temperatures for bin2 cases (0.3 mm < PWV < 0.5 mm) and those shown in Figure 10g are equivalent to a perturbation in the foreign continuum of 5.0%, 2.0%, and 3.0%, respectively, for the 675-, 850-, and 1,500-GHz microwindows. Therefore, we assign these values to the uncertainty in the foreign continuum due to the uncertainty in the water vapor profiles.
3. The radiometric uncertainty in the calibration of the SAO-FTS spectra, based on the error estimates for the responsivity calibration and reference load temperature given in Paine and Turner (2013), corresponds to an uncertainty in the foreign continuum of 14%, 8%, and 6% in the 675-, 850-, and 1,500-GHz microwindows, respectively.
4. The interquartile range of the residuals shown in panels d and g of Figure 10 also may indicate additional uncertainty in the derived continuum, although it is possible that this range may be to some extent attributable to the factors already analyzed above. To be conservative, we consider this to be an independent term in the uncertainty budget for the foreign continuum. The interquartile ranges in brightness temperature correspond to a change in foreign continuum of 5% for all three microwindows.

We assume these uncertainties are independent and add them in quadrature, resulting in a total uncertainty of the foreign continuum in the 675-, 850-, and 1,500-GHz microwindows of 18%, 12%, and 12%, respectively.

Foreign continuum absorption coefficients and associated uncertainty values for the sub-mm region (as well as other spectral regions, discussed below) are summarized in Table 5. The above uncertainty analysis for the sub-mm treats each microwindow as independent. However, the MT_CKD_v3.0 continuum coefficients that resulted from this study are derived from a curve that smoothly connects the spectral elements for which we have been able to evaluate the continuum strength. This provides an additional constraint on the continuum values, so the actual uncertainty of the foreign continuum may be less than the values provided in Table 5.

We perform one additional set of SAO-FTS calculations that is of interest. Instead of applying a PWV scale factor to each profile that was derived from a retrieval that operated on that profile, we scale all profiles with the identical factor, 1.05, close to the median scale factor in bins 1 and 2 in the analysis described above. (The use of a constant scale factor for all profiles parallels the approach used for the REFIR-PAD analysis.) Although for many cases this change in scaling approach does have a noticeable impact on the residuals in the sub-mm microwindows, the median residual in these microwindows does not change significantly. This provides evidence that median PWV that is used for the continuum determination is of critical importance in deriving the continuum in these microwindows, with the PWV values used for each individual case mattering to a lesser degree.

With respect to the determination of the uncertainty of the foreign continuum in 240–400 cm^{-1}, the region of the far-IR in which the bin2 REFIR-PAD measurements in RHUBC-II have significant sensitivity to the foreign continuum, the significant interquartile range of the final measurement-calculation residuals shown in Figure 6d (i.e., using Post-RII) requires careful consideration. Based on the sensitivity analysis shown in Figure 2c, the interquartile range of radiance residuals in Figure 6d corresponds to a change in the foreign continuum of 25–40%. Given the range of PWV scale factors derived in the SAO-FTS analysis, it is reasonable to speculate that a decent fraction of the variability in measurement-calculation residuals in far-IR microwindows could be explained by the water vapor profiles used in the LBLRTM calculations not utilizing these scale factors. However, for concurrent cases, the REFIR-PAD-vs-LBLRTM residuals have no appreciable correlation with the PWV scale factors derived in the SAO-FTS analysis. Instead, we believe that the cause of the large variability in the residuals is the random errors present in the REFIR-PAD measurements, which are larger than those encountered in the laboratory, due to the challenging environmental conditions (i.e., high winds) under which the instrument operated during the campaign.

As stated above, the interquartile range of the residuals between the REFIR-PAD and LBLRTM (with Post-RII) corresponds to a 25–40% change in the foreign continuum. However, we do not believe that it is appropriate to directly attribute a foreign continuum uncertainty of this magnitude to the residual variability in this region (as was done in the sub-mm uncertainty analysis above). Including such a term in the error budget, which would be large enough to dominate the budget, would disregard the significance of the consistency between the REFIR-PAD and SAO-FTS analyses. As discussed above, the 7% PWV scaling applied to the TI-sounding water vapor profiles for the far-IR analysis is consistent with the median 5% scaling determined by the SAO analysis (Table 2). This agreement between two independent assessments of the PWV gives confidence to each assessment. Since the derived continuum depends to a large extent on the median water vapor column amount, the agreement of PWV scale factors allows confidence in the sub-mm analysis to be transferred to the far-IR analysis, thereby mitigating the impact of the high variability of the far-IR residuals on our uncertainty analysis. Therefore, instead of computing an error budget for the 240- to 400-cm^{-1} region as was done for the sub-mm, we tie the uncertainty in the far-IR to the uncertainty in the sub-mm. However, we account for the higher variability of the far-IR residuals by assigning an additional 50% increase in uncertainty to the average uncertainty in the sub-mm microwindows, resulting in a 21% uncertainty in this region.

In the spectral region (80–210 cm^{-1}) in which neither the RHUBC-II REFIR-PAD nor SAO-FTS measurements have sensitivity to the foreign continuum, MT_CKD_3.0 has smoothly connected the continuum values determined outside this region. Given that the continuum values in this spectral region are from this fit rather than being based on observations in this region, we estimate the continuum uncertainty in this region at 30% based on alternate attempts to connect the continuum between the neighboring region on each side and the respective continuum uncertainties in these regions.

Table 5
MT_CKD_3.0 Foreign Continuum Coefficients and Associated Uncertainties in Microwave, Sub-mm, and Far-IR Regions

Wavenumber (cm^{-1})	MT_CKD_3.0 $(cm^{-1}\cdot mol\cdot cm^{-2})^{-1}$	Uncertainty (%)
0	9.31E−23	4
10	9.38E−23	10
20	9.41E−23	18
30	9.97E−23	12
40	1.17E−22	12
50	1.38E−22	12
60	1.54E−22	15
70	1.51E−22	18
80	1.39E−22	21
90	1.22E−22	25
100	1.06E−22	30
110	9.15E−23	30
120	8.01E−23	30
130	6.97E−23	30
140	6.05E−23	30
150	5.24E−23	30
160	4.56E−23	30
170	3.76E−23	30
180	3.05E−23	30
190	2.56E−23	30
200	2.20E−23	30
210	1.81E−23	30
220	1.48E−23	27
230	1.16E−23	24
240	8.77E−24	21
250	7.10E−24	21
260	5.90E−24	21
270	5.17E−24	21
280	4.19E−24	21
290	3.40E−24	21
300	2.68E−24	21
310	2.06E−24	21
320	1.84E−24	21
330	1.46E−24	21
340	1.09E−24	21
350	8.49E−25	21
360	6.42E−25	21
370	4.80E−25	21
380	3.80E−25	21
390	2.94E−25	14
400	2.22E−25	7
410	1.97E−25	7
420	1.68E−25	7
430	1.50E−25	7
440	1.34E−25	7
450	1.11E−25	7
460	9.66E−26	7
470	8.73E−26	7
480	7.47E−26	7
490	6.30E−26	7
500	5.31E−26	7
510	4.83E−26	7
520	4.21E−26	7
530	3.61E−26	7
540	3.06E−26	7
550	2.67E−26	7
560	2.30E−26	7
570	1.97E−26	7

Finally, in the 400- to 600-cm^{-1} region, the foreign continuum is based mainly on the NSA AERI-ER analysis. Although the REFIR-PAD measurements in RHUBC-II were not as sensitive to the continuum as the NSA AERI-ER measurements, the improvement in the microwindow residuals in this region shown in Figure 6 provides additional confidence to continuum values derived from the NSA AERI-ER results analysis. In this analysis, the uncertainty in the PWV is 2% (Delamere et al., 2010), which corresponds to a continuum uncertainty of 2–4% in this region. The IQR of the residuals shown in Figure 9d corresponds to an uncertainty in the continuum ranging from 3% at 400 cm^{-1} to 5% at 550 cm^{-1}. The final significant term in the continuum error budget in this region relates to the judgment that radiative closure has been achieved after spectroscopic values have been adjusted. As discussed above, we consider that the final residuals in Delamere et al. (2010) were less than optimal, particularly between 500 and 550 cm^{-1}. The difference between our perspective on the radiative closure of that data set and the perspective of the previous study should be considered an uncertainty in the continuum coefficients derived in the current study, which we estimate at 4%. Considering all these terms, we estimate the continuum uncertainty between 400 and 600 cm^{-1} to be 7%.

5. Impact of Spectroscopic Improvements

The modifications to spectroscopic parameters resulting from this study are somewhat larger and more extensive than those derived in the Delamere et al. (2010) study. Figure 2 of Turner, Merrelli, et al. (2012) showed the net flux differences resulting from the continuum modifications in Delamere et al. (2010), as well as other modifications to the MT_CKD continuum, were as high as 0.9 W/m^2 in the midtroposphere. Turner, Merrelli, et al. (2012) further showed that these continuum changes, when implemented in a fast radiation code used in a GCM, contributed to significant changes in the mean temperature, humidity, and cloud fields in a 20-year global simulation.

Figure 13 shows the changes in net, up, and down longwave flux that result from the spectroscopic improvements derived from the analysis presented herein (i.e., Post-RII vs. Pre-RII) for three atmospheric profiles (PWVs: tropical = 43.3 mm; U.S. standard = 15.1 mm; subarctic winter = 4.33 mm). The maximum change in net flux is 0.65–0.75 W/m^2 and occurs between 350 and 500 mb, depending on the atmospheric profile. This maximum is slightly smaller in magnitude and higher up in the atmosphere than the maximum net flux change in Delamere et al. (2010). We expect (but do not analyze here) that the new spectroscopic modifications will also lead to significant changes in climate simulations. Since the MT_CKD_3.0 far-IR foreign continuum below 400 cm^{-1} reverses some or all of continuum modifications that resulted from the Delamere et al. (2010) study, the flux differences between the updated spectroscopy (Post-RII) and the values employed prior to Delamere et al. (2010; not shown in Figure 13) are less than those shown in Figure 13.

The spectral distribution of the net flux changes is shown in Figure 14 and can be compared to Figure 17 in Delamere et al. (2010). (Note: In that figure in Delamere et al. (2010), the *y* axis is incorrect: The quantity actually plotted is 100xFlux.) In the midtroposphere (521 mb), the largest changes are for the subarctic winter (SAW) profile, consistent with the spectrally

Table 5
(continued)

Wavenumber (cm^{-1})	MT_CKD_3.0 $(cm^{-1}\cdot mol\cdot cm^{-2})^{-1}$	Uncertainty (%)
580	1.63E−26	7
590	1.37E−26	7
600	1.17E−26	7

integrated behavior shown in Figure 13, and occur mainly in the 250- to 350-cm^{-1} region. For the moister atmospheres shown, this spectral region is more opaque at this pressure, and the net flux changes of significance shift to higher wavenumbers. Higher up (286 and 194 mb) in the SAW profile the atmosphere is too transparent for the spectroscopic changes to significantly modify the net flux values, although non-negligible changes occur at various locations between 250 and 500 cm^{-1}. For the tropical (TRP) profile, notably large changes in net flux at 286 mb are seen between 200 and 325 cm^{-1}.

Changes in the vertical profiles of thermal heating rates resulting from the spectroscopic improvements in this study are shown in Figure 15. These are comparable in magnitude to the heating rate changes analyzed in Turner, Merrelli, et al., 2012; see Figure 2 of that paper), so we expect the new spectroscopic parameters derived in this study will also give rise to notable differences in GCM simulations.

6. Summary and Discussion

The conditions that characterized the RHUBC-II campaign, held in 2009, provided opacities low enough to evaluate the quality of spectroscopic parameters in the far-IR and sub-mm that had not been previously comprehensively assessed. Although this is primarily due to the extremely low water vapor abundances common at the campaign's desert site in the Atacama, the low surface pressure at this high-altitude location also contributed to the low opacity due to smaller pressure broadening of absorption lines and reduced water vapor continuum optical depths, which linearly depend on pressure. Exploiting these conditions, we analyzed the spectrally resolved far-IR and sub-mm radiances measured during this campaign in the wings of normally opaque lines and between these lines, deriving values for the foreign continuum and air-broadened line widths in these regions. When used in a validation exercise with FIRST measurements, which is an independent measurement data set from RHUBC-II, the derived spectroscopic parameters result in significantly improved residuals. A subsequent study by Rizzi et al. (2018) confirmed, based on an analysis of a separate observational data set collected by the REFIR-PAD in Antarctica, that the new spectroscopic parameters

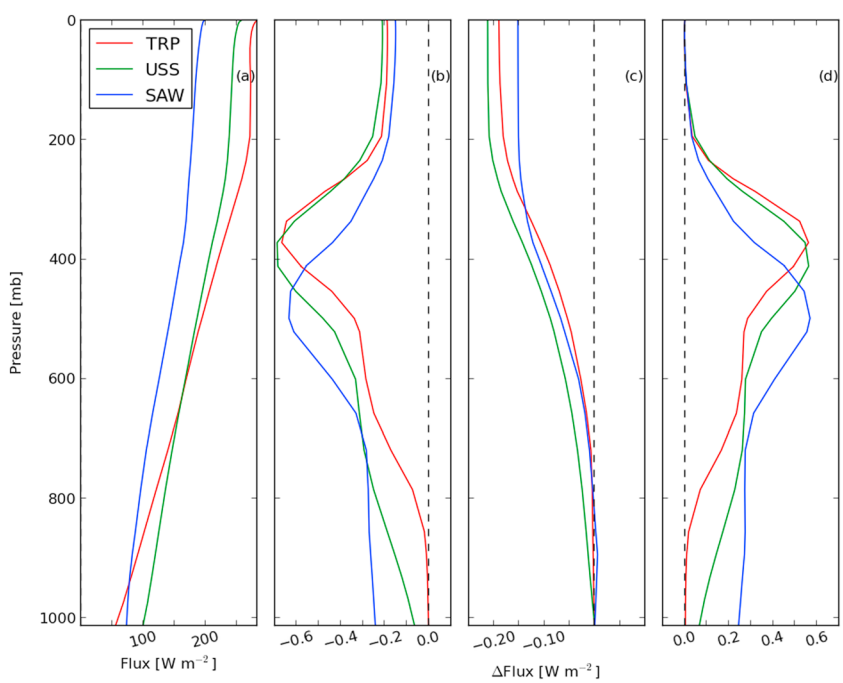

Figure 13. For 10–2000 cm^{-1}, (a) net flux computed by LBLRTM using Post-RII for the tropical, U.S. standard, and subarctic winter profiles; (b) change in net flux due to spectroscopic improvements in this study (Post-RII vs. Pre-RII); (c) change in up flux; and (d) change in down flux.

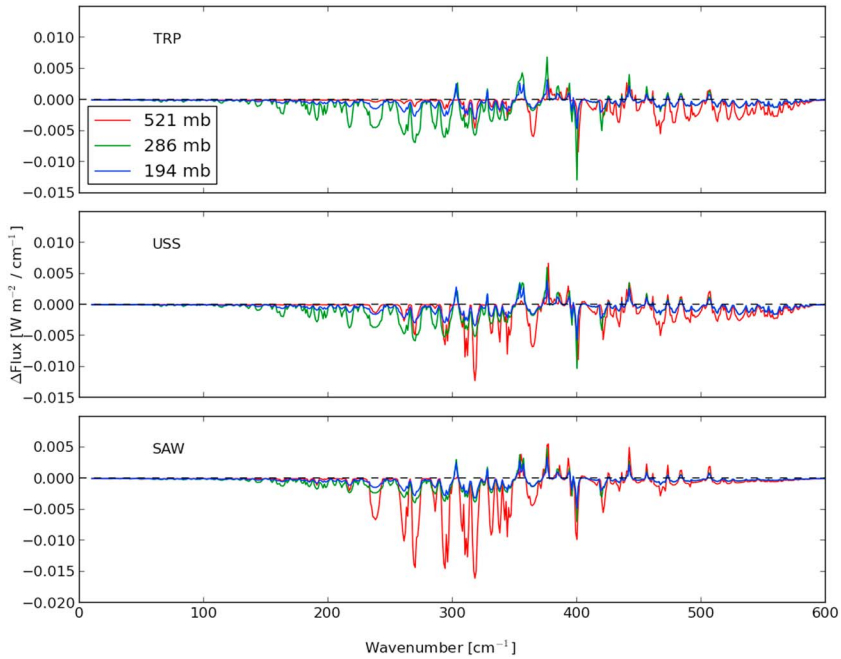

Figure 14. Change in spectral net flux from 0–600 cm^{-1} at three pressures between LBLRTM calculations using Post-RII with respect to calculations using Pre-RII for the (top) tropical, (middle) U.S. standard, and (bottom) subarctic winter profiles.

"substantially improved the modeling of water vapor absorption in the far-infrared." The improved spectroscopy results in significant modifications to computed values of thermal fluxes and heating rates (Figures 13 and 15) that are likely to impact climate simulations by GCMs.

The net effect of the analysis of observations from both RHUBC campaigns on the foreign continuum in the far-IR and sub-mm can be seen in Figure 7 by comparing MT_CKD_3.0 and MT_CKD_1.2. The new continuum is lower below 240 cm^{-1}, but to a lesser extent than had been deduced after RHUBC-I by Delamere et al. (2010; i.e., MT_CKD_2.4). MT_CKD_3.0 is greater than MT_CKD_1.2 above 240 cm^{-1}, with a further increase above 400 cm^{-1} than had been implemented after RHUBC-I, but for 240–400 cm^{-1} the RHUBC-II analysis has reversed the sign of the continuum change determined as a result of RHUBC-I. The impact on fluxes and heating rates of the continuum change from before RHUBC-I to after RHUBC-II (i.e., from MT_CKD_1.2 to MT_CKD_3.0) can be seen in Figures 16 and 17. The change in downwelling flux starts out negative in the upper troposphere due to the continuum decrease below 240 cm^{-1}, but lower down soon becomes positive for all atmospheres once radiation emitted in microwindows in the spectral region above 240 cm^{-1} starts to be appreciable. The change in downwelling flux peaks above 0.4 W/m^2 in the midtroposphere and remains at a considerable level at the surface in the subarctic winter profile, which is semitransparent at the surface at the high wavenumber end of the far-IR. The upward flux change can be as large as −0.2 W/m^2 and occurs in the upper troposphere. The change in net flux (Figure 16a) due to the combined effect of both RHUBC analyses are comparable to, but slightly smaller than, the net flux differences in the GCM study of Turner, Merrelli, et al., 2012; see Figure 2 in that paper), as are the heating rate changes due to both RHUBC analyses (Figure 17), suggesting that the spectroscopy improvements arising from the two RHUBC campaigns will have a beneficial and noticeable impact on climate prediction accuracy.

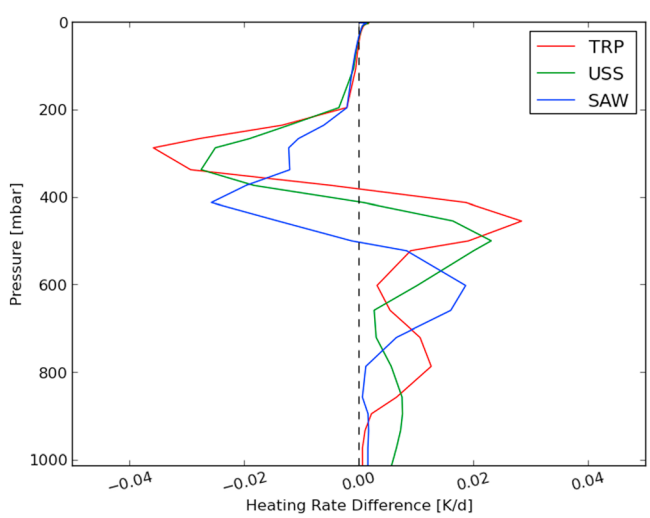

Figure 15. For 10–2000 cm^{-1}, change (Post-RII vs. Pre-RII) in heating rates computed by LBLRTM due to spectroscopic improvements in this study for the tropical, U.S. standard, and subarctic winter profiles.

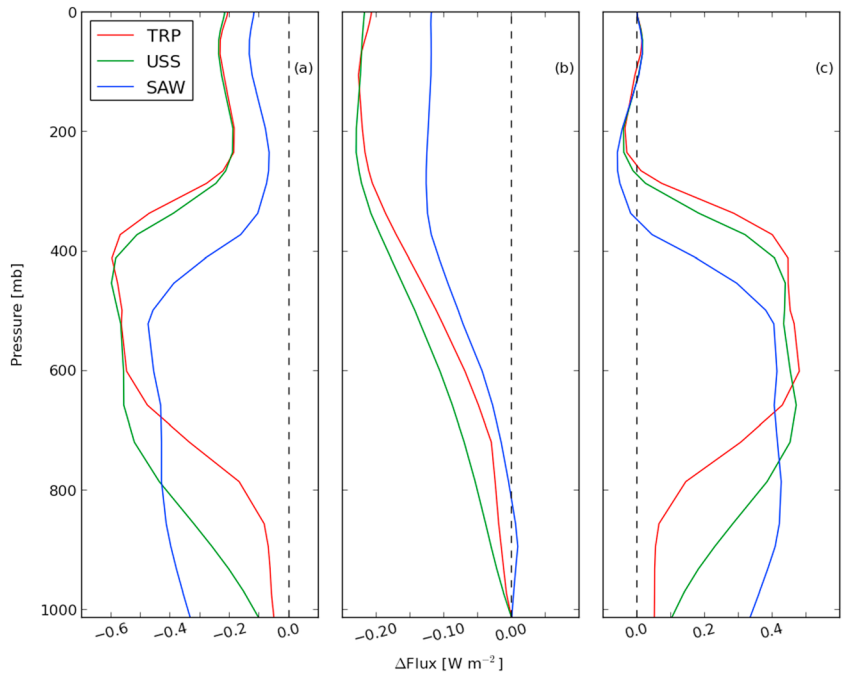

Figure 16. For 10–2000 cm^{-1}, (a) change in net flux computed by LBLRTM due to continuum changes resulting from the two Radiative Heating in Underexplored Bands Campaigns (MT_CKD_3.0 vs. MT_CKD_1.2, both calculations utilize the AER_v_2.2 linefile) for the tropical, U.S. standard, and subarctic winter profiles; (b) change in up flux; and (c) change in down flux.

The conditions that characterized the RHUBC-II campaign also presented impediments that worked against the campaign's objective of determining highly accurate values for the targeted spectroscopic parameters. Accurate water vapor profiles are essential in radiative closure studies like RHUBC-II, but in this campaign they were challenging to attain. Water vapor profiles from radiosondes have known and hard-to-correct accuracy issues in conditions of low humidity and low pressure. For RHUBC-II, the application of a well-regarded approach to correcting these inaccuracies in sonde water vapor measurements (Miloshevich et al., 2009) did not result in sufficiently accurate profiles, presumably due to the radiosondes not being representative of the column above the radiometric instruments. Exploiting the information on water vapor in GRVP measurements led to further improvement, but these profiles still were shown to have issues. Two independent additional methods were used to improve the GVRP-retrieved profiles, one based on sub-mm measurements and the other based on measurements in the 400- to 550-cm^{-1} region, which yielded results for the respective derived median scale factors that were consistent given the much larger uncertainties in the analysis. This consistency allows for some confidence in the profiles used in the sub-mm and far-IR closure studies, but still some residual skepticism in these profiles must remain. The small interquartile range of the residuals in the sub-mm analysis (Figures 6d and 6g), as well as the consistency of the results in the two lowest PWV bins (1 and 2), allow the derived spectroscopic parameters in this region to be viewed with a good amount of confidence. The higher variability of the far-IR residuals from 250–400 cm^{-1} do not allow the same degree of confidence.

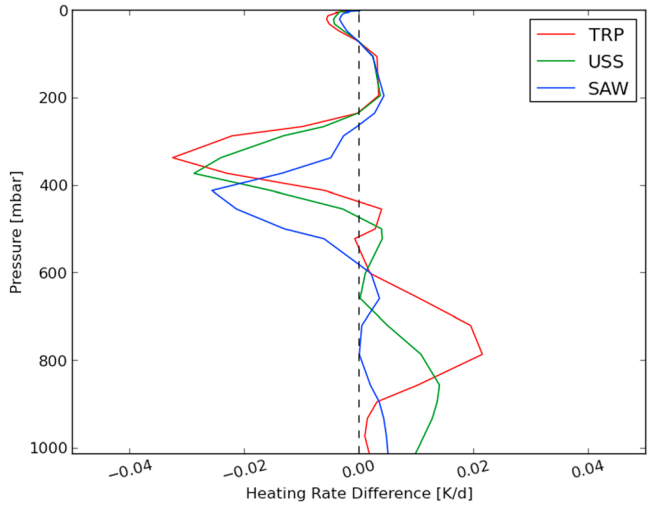

Figure 17. For 10–2000 cm^{-1}, change in heating rates computed by LBLRTM due to continuum changes resulting from the two Radiative Heating in Underexplored Bands Campaigns (MT_CKD_3.0 vs. MT_CKD_1.2, both calculations utilize the AER_v_2.2 linefile) for the tropical, U.S. standard, and subarctic winter profiles.

The analysis presented here is a significant step forward in investigating the behavior of dominant thermal radiative processes in the middle and upper troposphere that occur in the underexplored far-IR spectral

region. This advance is especially germane given the potential for two upcoming missions that will depend on a solid knowledge of far-IR spectroscopy, the National Aeronautics and Space Administration (NASA) Polar Radiant Energy in the Far-InfraRed Experiment and the ESA Far-infrared Outgoing Radiation Understanding and Monitoring (http://fts.fi.ino.it/forum). However, the uncertainties in the far-IR water vapor continuum coefficients determined in this study remain high, arguably a consequence of the challenging conditions that characterized the RHUBC-II campaign due to its remote and high-altitude location. In order for calculations of middle and upper tropospheric thermal fluxes and cooling rates to have the same confidence as lower tropospheric calculations, additional radiative closure studies and laboratory studies of the far-IR should be undertaken.

Acknowledgments
The RHUBC-II campaign was organized as part of the U.S. Department of Energy Atmospheric Radiation Measurement (ARM) program, which is sponsored by the Office of Science, Office of Biological and Environmental Research, Climate and Environmental Sciences Division. RHUBC-II was also supported in part by NASA, the Italian National Research Council, the Smithsonian Institution, and the German Science Foundation (DFG). The authors wish to thank the many members of the ARM program who contributed to the success of the RHUBC-II campaign. Special thanks go to Kim Nitschke and his team for organizing the logistical aspects of the campaign, and Kim and Jim Mather for the roles they played in choosing the site location. We thank Tim Wagner and Dave Tobin for each acting as lead site scientist for part of the campaign, and Alex Carizo for the invaluable role he filled in RHUBC-II operations and interfacing with local personnel and vendors. We also thank the staff at AstroNorte. We thank the NASA FIRST team during RHUBC-II, which included Rich Cageao, Glenn Farnsworth, Mike Wojcik, Jason Swasey, Joe Lee, Erik Syrstad, and Dave Johnson. We thank Bob Knuteson, Hank Revercomb, Dave Tobin, and Joe Taylor for their expertise on AERI spectral calibration and quality control. We would also like to acknowledge the many other people who contributed to the campaign and the collection of the data sets on the campaign: Charles Brinkmann, Troy Culgan, Mike Ryzcek, Julio Marin, Arlette Chacon, Toufic Hawat, Huabai Li, Marcos Diaz, Francesco Castagnoli, Denny Hackel, Ray Garcia, and Rich Coulter. We also thank the many people who shared their expertise with respect to the Atacama region that benefitted our planning for RHUBC-II: Humberto Fuenzalida, Simon Radford, José Rutllant, Lyman Page, Anthony Beasley, Monica Rubio, Michel Curé, David Rabanus, and Miguel González. We thank three anonymous reviewers for their insightful comments and suggestions. All RHUBC-II radiometric measurements and the temperature and moisture profiles used in the analysis are available at https://www.nssl.noaa.gov/users/dturner/public_html/papers/datasets/index.html and the ARM RHUBC-II data archive. Work on the study at AER was supported by the U.S. Department of Energy through contracts DE-FG02-90ER61064 and DE-SC0008618 and subcontract 331K203 from the University of Wisconsin, Dr. Turner's efforts were supported by grant DOE via grant DE-

References

Ackerman, T. P., & Stokes, G. M. (2003). The Atmospheric Radiation Measurement program. *Physics Today*, *56*, 38–44.

Birk, M., & Wagner, G. (2012). Temperature-dependent air broadening of water in the 1250–1750 cm $^{-1}$ range. *Journal of Quantitative Spectroscopy and Radiative Transfer*, *113*(11), 889–928. https://doi.org/10.1016/j.jqsrt.2011.12.013

Cadeddu, M. P., Liljegren, J. C., & Pazmany, A. L. (2007). Measurements and retrievals from a new 183-GHz water-vapor radiometer in the Arctic. *IEEE Transactions on Geoscience and Remote Sensing*, *45*(7), 2207–2215. https://doi.org/10.1109/TGRS.2006.888970

Campbell, J. R., Hlavka, D. L., Welton, E. J., Flynn, C. J., Turner, D. D., Spinhirne, J. D., et al. (2002). Full-time, eye-safe cloud and aerosol lidar observations at Atmospheric Radiation Measurement program sites: Instruments and data processing. *Journal of Atmospheric and Oceanic Technology*, *19*(4), 431–442. https://doi.org/10.1175/1520-0426(2002)019<0431:FTESCA>2.0.CO;2

Canas, A. A., Murray, J. E, & Harries, J. E. (1997). The Tropospheric Airborne Fourier Transform Spectrometer. Satellite Remote Sensing of Clouds and the Atmosphere II. In J. D. Haigh (Ed.), *International Society for Optical Engineering (SPIE Proceedings)* (Vol. 3220, pp. 91–102).

Cimini, D., Nasir, F., Westwater, E. R., Payne, V. H., Turner, D. D., Mlawer, E. J., et al. (2009). Comparison of ground-based millimeter-wave observations in the Arctic winter. *IEEE Transactions on Geoscience and Remote Sensing*, *47*(9), 3098–3106. https://doi.org/10.1109/TGRS.2009.2020743

Cimini, D., Rosenkranz, P. W., Tretyakov, M. Y., Koshelev, M. A., & Romano, F. (2018). Uncertainty of atmospheric microwave absorption model: impact on ground-based radiometer simulations and retrievals. *Atmospheric Chemistry and Physics*, *18*(20), 15,231–15,259. https://doi.org/10.5194/acp-18-15231-2018

Clerbaux, C., Hadji-Lazaro, J., Turquety, S., George, M., Coheur, P.-F., Hurtmans, D., et al. (2007). The IASI/MetOp1 Mission: First observations and highlights of its potential contribution to GMES2. *Space Research Today*, *168*, 19–24. https://doi.org/10.1016/S0045-8732(07)80046-5

Clough, S. A., Kneizys, F. X., & Davies, R. W. (1989). Line shape and the water vapor continuum. *Atmospheric Research*, *23*(3-4), 229–241. https://doi.org/10.1016/0169-8095(89)90020-3

Clough, S. A., Shephard, M. W., Mlawer, E. J., Delamere, J. S., Iacono, M. J., Cady-Pereira, K., et al. (2005). Atmospheric radiative transfer modeling: A summary of the AER codes. *Journal of Quantitative Spectroscopy & Radiative Transfer*, *91*(2), 233–244. https://doi.org/10.1016/j.jqsrt.2004.05.058

Clough, S. A., Shephard, M. W., Worden, J., Brown, P. D., Worden, H. M., Luo, M., et al. (2006). Forward model and Jacobians for tropospheric emission spectrometer retrievals. *IEEE Transactions on Geoscience and Remote Sensing*, *44*(5), 1308–1323. https://doi.org/10.1109/TGRS.2005.860986

Coudert, L., Wagner, H., Birk, G., Baranov, M., Yu, I., Lafferty, W. J., & Flaud, J.-M. (2008). The H16O molecule: Line poisition and 2 line intensity analyses up to the second triad. *Journal of Molecular Spectroscopy*, *251*(1-2), 339–357. https://doi.org/10.1016/j.jms.2008.03.021

Delamere, J. S., Clough, S. A., Payne, V., Mlawer, E. J., Turner, D. D., & Gamache, R. (2010). A far-infrared radiative closure study in the Arctic: Application to water vapor. *Journal of Geophysical Research*, *115*(D17), D17106. https://doi.org/10.1029/2009JD012968

Fox, C., Green, P., Pickering, J., & Humpage, N. (2015). Analysis of far-infrared spectral radiance observations of the water vapor continuum in the Arctic. *Journal of Quantitative Spectroscopy and Radiation Transfer*, *155*, 57–65. https://doi.org/10.1016/j.jqsrt.2015.01.001

Gordon, I., Rothman, L., Gamache, R., Jacquemart, D., Boone, C., Bernath, P., et al. (2007). Current updates of the water-vapor line list in HITRAN: A new "diet" for air-broadened half-widths. *Journal of Quantitative Spectroscopy & Radiative Transfer*, *108*(3), 389–402. https://doi.org/10.1016/j.jqsrt.2007.06.009

Green, P. D., Newman, S. M., Beeby, R. J., Murray, J. E., Pickering, J. C., & Harries, J. E. (2012). Recent advances in measurement of the water vapour continuum in the far-infrared spectral region. *Philosophical Transactions. Series A, Mathematical, Physical, and Engineering Sciences*, *370*(1968), 2637–2655. https://doi.org/10.1098/rsta.2011.0263

Harries, J., Carli, B., Rizzi, R., Serio, C., Mlynczak, M., Palchetti, L., et al. (2008). The far-infrared Earth. *Reviews of Geophysics*, *46*, RG4004. https://doi.org/10.1029/2007RG000233

Hartmann, J.–. M., Boulet, C., & Robert, D. (2008). *Collisional effects of molecular spectra* (p. 411). Amsterdam: Elsevier.

Hawat, T., Stephen, T., & Murcray, F. (2002). Absolute solartransmittance interferoemter for ground-based measurements. *Applied Optics*, *41*, 3582–3589.

Humlicek, J. (1972). Optimized computation of the Voigt and complex probability functions. *Journal of Quantitative Spectroscopy and Radiation Transfer*, *27*(4), 437–444. https://doi.org/10.1016/0022-4073(82)90078-4

Iacono, M. J., Mlawer, E. J., Clough, S. A., & Morcrette, J.-J. (2000). Impact of an improved longwave radiation model, RRTM, on the energy budget and thermodynamic properties of the NCAR community climate model, CCM3. *Journal of Geophysical Research*, *105*(D11), 14,873–14,890. https://doi.org/10.1029/2000JD900091

Knuteson, R. O., Revercomb, H. E., Best, F. A., Ciganovich, N. C., Dedecker, R. G., Dirkx, T. P., et al. (2004a). The Atmospheric Emitted Radiance Interferometer (AERI) Part I: Instrument design. *Journal of Atmospheric and Oceanic Technology*, *21*(12), 1763–1776. https://doi.org/10.1175/JTECH-1662.1

Knuteson, R. O., Revercomb, H. E., Best, F. A., Ciganovich, N. C., Dedecker, R. G., Dirkx, T. P., et al. (2004b). The Atmospheric Emitted Radiance Interferometer (AERI) Part II: Instrument performance. *Journal of Atmospheric and Oceanic Technology*, *21*(12), 1777–1789. https://doi.org/10.1175/JTECH-1663.1

SC0008830 and by NOAA, and Dr. Paine was supported by Smithsonian Institution Endowment Funds and the Smithsonian Astrophysical Observatory. Palchetti and Bianchini were supported by the Italian National Research Council-Earth System Science and Environmental Technologies-Institute of Applied Physics "Nello Carrara." Work at the Jet Propulsion Laboratory, California Institute of Technology, was carried out under a contract with the National Aeronautics and Space Administration. References herein to any specific commercial product, process or service by trade name, trademark, manufacturer or otherwise does not constitute or imply its endorsement by the United States Government or the Jet Propulsion Laboratory, California Institute of Technology. Support for the FIRST team was provided by the NASA Earth Science Technology Office for the FIRST recalibration effort and the Climate Absolute Radiance and Refractivity Observatory (CLARREO) preformulation project at NASA Langley Research Center for the FIRST field campaign data analyses.

Lamouroux, J., Regalia, L., Thomas, X., Vander Auwera, J., Gamache, R., & Hartmann, J.-M. (2015). CO_2 line-mixing database and software update and its tests in the 2.1 μm and 4.3 μm regions. *Journal of Quantitative Spectroscopy and Radiation Transfer*, *151*, 88–96. https://doi.org/10.1016/j.jqsrt.2014.09.017

Liu, Q., & Boukabara, S. (2014). Community Radiative Transfer Model (CRTM) applications in supporting the Suomi National Polar-orbiting Partnership (SNPP) mission validation and verification. *Remote Sensing of Environment*, *140*, 744–754. https://doi.org/10.1016/j.rse.2013.10.011

Liuzzi, G., Masiello, G., Serio, C., Palchetti, L., & Bianchini, G. (2014). Validation of water vapor continuum absorption models in the wave number range 180–600 cm^{-1} with atmospheric emitted spectral radiance measured at the Antarctica Dome-C site. *Optics Express*, *22*(14), 16,784–16,801. https://doi.org/10.1364/OE.22.016784

Ma, Q., Tipping, R. H, & Gamache, R. R. (2010). Uncertainties associated with theoretically calculated N2-broadened half-widths of H2O lines. *Molecular Physics*, *108*(17), 2225–2252. https://doi.org/10.1080/00268976.2010.505209

Marín, J. C., Pozo, D., Mlawer, E., Turner, D. D., & Curé, M. (2013). Dynamics of Local Circulations in Mountainous Terrain during the RHUBC-II Project. *Monthly Weather Review*, *141*(10), 3641–3656. https://doi.org/10.1175/MWR-D-12-00245.1

Mast, J. C., Mlynczak, M. G., Cageao, R. P., Kratz, D. P., Latvakoski, H., Johnson, D. G., et al. (2017). Measurements of downwelling far-infrared radiance during the RHUBC-II campaign at Cerro Toco, Chile and comparisons with line-by-line radiative transfer calculations. *Journal of Quantitative Spectroscopy and Radiation Transfer*, *198*, 25–39. https://doi.org/10.1016/j.jqsrt.2017.04.028

Miloshevich, L., Vomel, H., Whiteman, D., & Leblanc, T. (2009). Accuracy assessment and correction of Vaisala RS92 radiosonde water vapor measurements. *Journal of Geophysical Research*, *114*(D11), D11305. https://doi.org/10.1029/2008JD011565

Mlawer, E. J., Iacono, M. J., Pincus, R., Barker, H. W., Oreopoulos, L., & Mitchell, D. L. (2016). Contributions of the ARM Program to Radiative Transfer Modeling for Climate and Weather Applications. *Meteorological Monographs*, *57*, 15.1–15.19. https://doi.org/10.1175/amsmonographs-d-15-0041.1

Mlawer, E. J., Payne, V. H., Moncet, J.-L., Delamere, J. S., Alvarado, M. J., & Tobin, D. C. (2012). Development and recent evaluation of the MT_CKD model of continuum absorption. *Philosophical Transactions of the Royal Society A*, *370*(1968), 2520–2556. https://doi.org/10.1098/rsta.2011.0295

Mlawer, E. J., Taubman, S. J., Brown, P. D., Iacono, M. J., & Clough, S. A. (1997). Radiative transfer for inhomogeneous atmospheres: RRTM, a validated correlated-k model for the longwave. *Journal of Geophysical Research*, *102*(D14), 16,663–16,682. https://doi.org/10.1029/97JD00237

Mlawer, E. J., & Turner, D. D. (2016). Spectral radiation measurements and analysis in the ARM Program. *Meteorological Monographs*, *57*, 14.1–14.17. https://doi.org/10.1175/amsmonographs-d-15-0027.1

Mlynczak, M. G., Johnson, D. G., Latvakoski, H., Jucks, K., Watson, M., Kratz, D. P, & Liu, X. (2006). First light from the Far-Infrared Spectroscopy of the Troposphere (FIRST) instrument. *Geophysical Research Letters*, *33*, L07704. https://doi.org/10.1029/2005GL025114

Niro, F., Jucks, K., & Hartmann, J.-M. (2005). Spectral calculations in central and wing regions of CO2 IR bands. IV: Software and database for the computation of atmospheric spectra. *Journal of Quantitative Spectroscopy & Radiative Transfer*, *95*(4), 469–481. https://doi.org/10.1016/j.jqsrt.2004.11.011

Oreopoulos, L., Mlawer, E., Delamere, J., Shippert, T., Cole, J., Fomin, B., et al. (2012). The continual intercomparison of radiation codes: Results from phase I. *Journal of Geophysical Research*, *117*(D6), D06118. https://doi.org/10.1029/2011JD016821

Paine, S. (2017). The *am* Atmospheric Model (v. 9.2), *Zenodo*. https://doi.org/10.5281/zenodo.438726

Paine, S., Blundell, R., Papa, D. C., Barrett, J. W., & Radford, S. J. E. (2000). A Fourier Transform spectrometer for measurement of atmospheric transmission at submillimeter wavelengths. *Proceedings Astronomical Society of the Pacific*, *112*(767), 108–118. https://doi.org/10.1086/316497

Paine, S., & Turner, D. D. (2013). Processing and calibration of submillimeter Fourier Transform radiometer spectra from the RHUBC-II Campaign. *IEEE Transactions on Geoscience and Remote Sensing*, *51*(12), 5187–5198. https://doi.org/10.1109/TGRS.2012.2231869

Palchetti, L., Bianchini, G., Carli, B., Cortesi, U., & Del Bianco, S. (2008). Measurement of the water vapor vertical profile and of the Earth's outgoing far infrared flux. *Atmospheric Chemistry and Physics*, *8*(11), 2885–2894. https://doi.org/10.5194/acp-8-2885-2008

Palchetti, L., Bianchini, G., Castognoli, F., Carli, B., Serio, C., Esposito, F., et al. (2005). Breadboard of the Fourier transform spectrometer for the Radiation Explorer in the Far Infrared (REFIR) atmospheric mission. *Applied Optics*, *44*(14), 2870–2878. https://doi.org/10.1364/AO.44.002870

Payne, V. H., Delamere, J. S., Cady-Pereira, K. E., Gamache, R. R., Moncet, J.-L., Mlawer, E. J., & Clough, S. A. (2008). Air-broadened half-widths of the 22 and 183 GHz water vapor lines. *IEEE Transactions on Geoscience and Remote Sensing*, *46*(11), 3601–3617. https://doi.org/10.1109/TGRS.2008.2002435

Payne, V. H., Mlawer, E. J., Cady-Pereira, K. E., & Moncet, J.-L. (2011). Water vapor continuum absorption in the microwave. *IEEE Transactions on Geoscience and Remote Sensing*, *49*(6), 2194–2208. https://doi.org/10.1109/TGRS.2010.2091416

Pincus, R., Mlawer, E. J., Oreopoulos, L., Ackerman, A. S., Baek, S., Brath, M., et al. (2015). Radiative flux and forcing parameterization error in aerosol-free clear skies. *Journal of Geophysical Research: Letters*, *42*(13), 5485–5492. https://doi.org/10.1002/2015GL064291

Revercomb, H. E., Turner, D. D., Tobin, D. C., Knuteson, R. O., Feltz, W. F., Barnard, J., et al. (2003). The Atmospheric Radiation Measurement Program's water vapor intensive observation periods: overview, initial accomplishments, and future challenges. *Bulletin of the American Meteorological Society*, *84*(2), 217–236. https://doi.org/10.1175/BAMS-84-2-217

Rizzi, R., Maestri, T., & Arosio, C. (2018). Estimate of radiosonde dry bias from far-infrared measurements on the Antarctic plateau. *Journal of Geophysical Research: Atmospheres*, *123*, 3205–3211. https://doi.org/10.1002/2017JD027874

Rothman, L. S., Gordon, I. E., Babikov, Y., Barbe, A., Chris Benner, D., Bernath, P. F., et al. (2013). The HITRAN 2012 molecular spectroscopic database. *Journal of Quantitative Spectroscopy and Radiation Transfer*, *130*, 4–50. https://doi.org/10.1016/j.jqsrt.2013.07.002

Rothman, L. S., Gordon, I. E., Barbe, A., Benner, D. C., Bernath, P. F., Birk, M., et al. (2009). The HITRAN 2008 molecular spectroscopic database. *Journal of Quantitative Spectroscopy and Radiation Transfer*, *110*(9-10), 533–572. https://doi.org/10.1016/j.jqsrt.2009.02.013

Rutllant Costa, J. (1977). On the extreme aridity of coastal and Atacama deserts in northern Chile, Ph.D. dissertation, Univ. Wisconsin – Madison.

Serio, C., Masiello, G., Esposito, F., di Girolamo, P., di Iorio, T., Palchetti, L., et al. (2008). Retrieval of foreign-broadened water vapor continuum coefficients from emitted spectral radiance in the water vapor rotational band from 240 to 590 cm^{-1}. *Optics Express*, *16*(20), 15,816–15,833. https://doi.org/10.1364/OE.16.015816

Shi, S.-C., Paine, S., Yao, Q. J., Lin, Z. H., Li, X. X., Duan, W. Y., et al. (2016). Terahertz and far-infrared windows opened at Dome A in Antarctica. *Nature Astronomy*, *1*(1), 1–7. https://doi.org/10.1038/s41550-016-0001

Stokes, G. M., & Schwartz, S. E. (1994). The Atmospheric Radiation Measurement (ARM) program: Programmatic background and design of the cloud and radiation test bed. *Bulletin of the American Meteorological Society*, *75*, 1201–1221.

Sussmann, R., Reichert, A., & Rettinger, M. (2016). The Zugspitze radiative closure experiment for quantifying water vapor absorption over the terrestrial and solar infrared – Part 1: Setup, uncertainty analysis, and assessment of far-infrared water vapor continuum. *Atmospheric Chemistry and Physics*, *16*(18), 11,649–11,669. https://doi.org/10.5194/acp-16-11649-2016

Tobin, D. C., Best, F. A., Brown, P. D., Clough, S. A., Dedecker, R. G., Ellingson, R. G., et al. (1999). Downwelling spectral radiance observations at the SHEBA ice station: Water vapor continuum measurements from 17-26 micrometer. *Journal of Geophysical Research*, *104*, 2081–2092.

Troyan, D. (2012). Merged sounding value-added product. https://www.arm.gov/publications/tech_reports/doe-sc-arm-tr-087.pdf

Turner, D. D., & Ellingson, R. G. (2016). Introduction. *Meteorological Monographs*, *57*, v–x. https://doi.org/10.1175/amsmonographs-d-16-0001.1

Turner, D. D., & Blumberg, W. G. (2018). Improvements to the AERIoe Thermodynamic Profile Retrieval Algorithm. *IEEE Journal of Selected Topics in Applied Earth Observations and Remote Sensing*, 1–16. https://doi.org/10.1109/jstars.2018.2874968

Turner, D. D., & Löhnert, U. (2014). Information content and uncertainties in thermodynamic profiles and liquid cloud properties retrieved from the ground-based Atmospheric Emitted Radiance Interferometer (AERI). *Journal of Applied Meteorology and Climatology*, *53*(3), 752–771. https://doi.org/10.1175/JAMC-D-13-0126.1

Turner, D. D., Merrelli, A., Vimont, D., & Mlawer, E. J. (2012). Impact of modifying the longwave water vapor continuum absorption model on community Earth system model simulations. *Journal of Geophysical Research*, *117*(D4), D04106. https://doi.org/10.1029/2011JD016440

Turner, D. D., & Mlawer, E. J. (2010). Radiative heating in underexplored bands campaigns (RHUBC). *Bulletin of the American Meteorological Society*, *91*(7), 911–924. https://doi.org/10.1175/2010BAMS2904.1

Turner, D. D., Mlawer, E. J., Bianchini, G., Cadeddu, M. P., Crewell, S., Delamere, J. S., et al. (2012). Ground-based high spectral resolution observations of the entire terrestrial spectrum under extremely dry conditions. *Geophysical Research Letters*, *39*, L10801. https://doi.org/10.1029/2012GL051542

Turner, D. D., Tobin, D. C., Clough, S. A., Brown, P. D., Ellingson, R. G., Mlawer, E. J., et al. (2004). The QME AERI LBLRTM: A closure experiment for downwelling high spectral resolution infrared radiance. *Journal of the Atmospheric Sciences*, *61*(22), 2657–2675. https://doi.org/10.1175/JAS3300.1

Van Vleck, J. H., & Huber, D. L. (1977). Absorption, emission and linebreadths: a semihistorical perspective. *Reviews of Modern Physics*, *49*(4), 939–959. https://doi.org/10.1103/RevModPhys.49.939

Verlinde, J., Zak, B. D., Shupe, M. D., Ivey, M. D., & Stamnes, K. (2016). The ARM North Slope of Alaska (NSA) Sites. *Meteorological Monographs*, *57*, 8.1–8.13. https://doi.org/10.1175/amsmonographs-d-15-0023.1

References From the Supporting Information

Bianchini, G., & Palchetti, L. (2008). Technical note: REFIR-PAD level 1 data analysis and performance characterization. *Atmospheric Chemistry and Physics*, *8*(14), 3817–3826. https://doi.org/10.5194/acp-8-3817-2008

Bianchini, G., Palchetti, L., & Carli, B. (2006). A wide-band nadir-sounding spectroradiometer for the characterization of the Earth's outgoing long-wave radiation. *Proceedings of SPIE*, *6361*, 63610A. https://doi.org/10.1117/12.689260

Bianchini, G., Palchetti, L., Muscari, G., Fiorucci, I., Di Girolamo, P., & Di Iorio, T. (2011). Water vapor sounding with the far infrared REFIR-PAD spectroradiometer from a high-altitude ground-based station during the ECOWAR campaign. *Journal of Geophysical Research*, *116*(D2), D02310. https://doi.org/10.1029/2010JD014530

Bianchini, G. F., Castagnoli, G., Di Natale, L., & Palchetti, L. (2019). A Fourier transform spectroradiometer for ground-based remote sensing of the atmospheric downwelling long-wave radiance. *Atmospheric Measurement Techniques*, *12*(1), 619–635. https://doi.org/10.5194/amt-12-619-2019

Cadeddu, M. P., Liljegren, J. C., & Turner, D. D. (2013). The Atmospheric Radiation Measurement (ARM) program network of microwave radiometers: Instruments, data, and retrievals. *Atmospheric Measurement Techniques*, *6*(9), 2359–2372. https://doi.org/10.5194/amt-6-2359-2013

Cady-Pereira, K. E., Shephard, M., Turner, D., Mlawer, E., Clough, S., & Wagner, T. (2008). Improved daytime precipitable water vapor from Vaisala radiosonde humidity sensors. *Journal of Atmospheric and Oceanic Technology*, *25*(6), 873–883. https://doi.org/10.1175/2007JTECHA1027.1

Dzambo, A. M., Turner, D. D., & Mlawer, E. J. (2016). Evaluation of two Vaisala RS92 radiosonde solar radiative dry bias correction algorithms. *Atmospheric Measurement Techniques*, *9*(4), 1613–1626. https://doi.org/10.5194/amt-9-1613-2016

Galewsky, J., Rella, C., Sharp, Z., Samuels, K., & Ward, D. (2011). Surface measurements of upper tropospheric water vapor isotopic composition on the Chajnantor Plateau, Chile. *Geophysical Research Letters*, *38*, L17803. https://doi.org/10.1029/2011GL048557

Genest, J., & Tremblay, P. (1999). Instrument line shape of Fourier transform spectrometers: analytic solutions for nonuniformly illuminated off-axis detectors. *Applied Optics*, *38*(25), 5438–5446. https://doi.org/10.1364/AO.38.005438

Palchetti, L., Belotti, C., Bianchini, G., Castagnoli, F., Carli, B., Cortesi, U., et al. (2016). Technical note: First spectral measurement of the Earth's upwelling emission using an uncooled wideband Fourier transform spectrometer. *Atmospheric Chemistry and Physics*, *6*, 5025–5030.

Revercomb, H. E., Buijs, H., Howell, H. B., LaPorte, D. D., Smith, W. L., & Sromovsky, L. A. (1988). Radiometric calibration of IR Fourier transform spectrometers: Solution to a problem with the High-Resolution Interferometer Sounder. *Applied Optics*, *27*(15), 3210–3218. https://doi.org/10.1364/AO.27.003210

Rodgers, C. D. (2000). *Inverse methods for atmospheric sounding*. Singapore: World Scientific. https://doi.org/10.1142/3171

Turner, D., Lesht, B., Clough, S., Liljegren, J., Revercomb, H., & Tobin, D. (2003). Dry bias and variability in Vaisala Radiosondes: The ARM experience. *Journal of Atmospheric and Oceanic Technology*, *20*(1), 117–132. https://doi.org/10.1175/1520-0426(2003)020<0117:DBAVIV>2.0.CO;2

Turner, D. D., Mlawer, E. J., & Revercomb, H. E. (2016). Water vapor observations in the ARM program. In *The Atmospheric Radiation Measurement Program: The First 20 Years*, *Meteor. Monograph* (Vol. 57, pp. 1311–1318). Boston: American Meteor Society. https://doi.org/10.1175/AMSMONOGRAPHS-D-15-0025.1